Computational Investigation of Biological Propulsion Systems at Low Reynolds Numbers

---

A Thesis

Presented to

the Faculty of the College of Engineering

Villanova University

In Partial Fulfillment

of the Requirements for the Degree

Master of Science in Mechanical Engineering

By

Seth Lionetti

March 2022

Abstract

In nature, animals rely on oscillatory motions of their propulsors to transport surrounding fluid and generate necessary forces for flying and swimming. For instance, small insects (e.g., hawkmoth, butterfly, fruit fly, and dragonfly) can achieve highly efficient flight and agile maneuvers by flapping their wings. Many small swimming organisms (e.g., ctenophores, copepods, krill, and shrimp) use coordinated arrays of appendages to create efficient hydrodynamic performance for long-distance locomotion. Studying these biological propulsion systems which fly/swim in a low Reynolds number regime can aid in the development of bio-inspired micro-size aerial vehicles and aquatic robots. The present project aims to examine biological locomotion and fluid dynamic mechanisms present in different small animal species. In order to achieve this, high-speed video recordings were used to generate 3D surface reconstructions of biological locomotion. The reconstructions were then imposed in an in-house immersed-boundary-method based computational fluid dynamics (CFD) solver. The CFD solver provided a quantitative measure of the force generation, power consumption, and vortex structures generated during sustained flying and swimming.

One animal simulated in this study is the hawkmoth *Manduca sexta*. Hawkmoths are large insects capable of long sequences of steady flight at lower speeds. Previous researchers have shown that hawkmoths are incapable of sustaining steady forward flight at speeds greater than 4m/s, about one-half of the theoretical prediction based on the insect's body mass. In order to explain what constrains hawkmoths' maximum forward flying speed, CFD simulations were run for hawkmoths flying at 0m/s, 2m/s, and 4m/s. Results show that the moth minimizes drag as flying speed increases, but it immediately

loses its lift producing upstroke even at slow forward flight speeds (2 m/s), and a significant amount of negative lift generated during the upstroke at higher forward flying speeds (4 m/s). This negative lift generation during the upstroke potentially reduces the hawkmoth's maximum sustained flight speed. The other species simulated in this study are ctenophores, the largest animals in the world that locomote via ciliary propulsion. Previous studies on ciliary propulsion have assumed the substrate in which the cilia are embedded is flat. However, in nature, the substrate of ciliated invertebrates is nontrivially curved. CFD results for ctenophore swimming show that having a curved substrate provides a 20% improvement in thrust generation compared to a flat substrate. Our simulation results aim to provide fundamental fluid dynamic principles for guiding the design of bio-inspired miniaturized flexible robots flying/swimming in the low-to-intermediate Reynolds number regime.

Acknowledgements

I would like to extend my deepest gratitude to my research advisor, Dr. Chengyu Li. His invaluable advice and guidance made this work possible. I also wish to thank Dr. Tyson Hedrick and Dr. Margaret Byron for their key contributions to this study. I have had the pleasure of working with Zhipeng Lou and Menglong Lei, whose assistance and expertise are greatly appreciated. I would like to express my gratitude to the Villanova University College of Engineering for providing me the opportunity to pursue this research. Finally, I would like to thank my family for their support.

Table of Contents

List of Figures

List of Tables

Nomenclature

Symbol	Description
3-D	Three dimensional
R	Wing span length
c	Mean wing chord length
ψ	Wing stroke angle
ϕ	Wing deviation angle
θ	Wing pitch angle
Φ	Stroke amplitude
β	Hawkmoth stroke plane angle
χ	Hawkmoth body incline angle
f	Beat frequency
U_{tip}	Tip velocity
$U_{tip,ave}$	Cycle-averaged tip velocity
U_{∞}	Hawkmoth forward flying speed
v	Kinematic viscosity
Re	Reynolds number
J	Advance ratio
S	Area of wing/ctene surface
F_D	Drag force
F_T	Thrust force

F_L	Lift force
P_{mech}	Mechanical power
P^*_{mech}	Mass-specific mechanical power
P_{iner}	Inertial power
P^*_{iner}	Mass-specific inertial power
P_{aero}	Aerodynamic power
P^*_{aero}	Mass-specific aerodynamic power
P_{hydro}	Hydrodynamic power
C_D	Drag coefficient
C_T	Thrust coefficient
C_L	Lift coefficient
C_F	Total force coefficient
C_{PW}	Hydrodynamic power coefficient
$\overline{C_D}$	Cycle-averaged drag coefficient
$\overline{C_T}$	Cycle-averaged thrust coefficient
$\overline{C_L}$	Cycle-averaged lift coefficient
$\overline{C_F}$	Cycle-averaged total force coefficient
$\overline{C_{PW}}$	Cycle-averaged hydrodynamic power coefficient
κ	Ctenophore body curvature
L_b	Ctenophore body length
U_b	Ctenophore body velocity
l	Average ctene length

P_L	Phase lag
$\overline{U_{tip}}$	Ctene tip velocity averaged between the middle eight ctenes
Re_b	Ctenophore body Reynolds number
Re_ω	Oscillatory Reynolds number

Chapter 1: Introduction

In the field of fluid dynamics, one particularly active area of study is the development of small robotic vehicles. Due to their size, such vehicles are capable of performing highly specialized tasks. For example, micro-aerial vehicles (MAVs) are remotely operable aircraft that are widely used for surveillance and aerial photography. In addition, small swimming robots can be used for targeted drug delivery, as well as other medicinal applications. These vehicles can range in size from less than a millimeter to several centimeters across. At such small scales, the development of maneuverable and efficient vehicles can be a challenge. Therefore, naturally occurring propulsion systems (such as those found in insects and small swimming animals) are often used as inspiration for artificial designs.

Insects and small swimming animals locomote at low-to-intermediate Reynolds numbers (*Re*). This means that both viscous forces and inertial forces play a role in propulsion. Small flying/swimming animals typically generate force by beating their propulsors. To better understand these propulsion mechanisms, this project aims to examine how flight speed affects insect aerodynamic performance and to explore the hydrodynamic performance of ciliary propulsion.

1.1 Unsteady Aerodynamics of Flapping-Wing Flight

As insects flap their wings, they create tornado-shaped leading-edge vortex (LEV) above the wing surface to generate sufficient aerodynamic force required to perform various flight tasks (Ellington, van den Berg et al. 1996). As a consequence, the unsteady flow evolves to a trail of aerodynamic footprints (complex vortex structures) in the wake.

Among all flight modes, the two most widely studied modes are hovering and forward flight due to their potential broader applications in man-made robotic designs. In order to achieve a sustained flight mode at a fixed position (hovering) or at a constant forward flight speed (cruising), insects need to adjust their wing movements to reach a force balance in both vertical and horizontal directions.

Previous studies have used several different methods to examine how insects' kinematics and aerodynamics change as their flight speed increases. Wilmott & Ellington (Dudley and Ellington 1990, Dudley and Ellington 1990) used high-speed cinematography and a force transducer to measure bumblebee wing kinematics and aerodynamic performance over a range of flight speeds (0 m/s-4.5 m/s). They found that as a bumblebee's forward flying speed increases, its wing angle of attack relative to the stroke plane also increases. In addition, during hovering flight, the bumblebee's downstroke and upstroke were shown to provide equal contributions to its total lift. However, as the bumblebee transitions to forward flight, its downstroke plays an increasingly dominant role in lift production. Zhu & Sun (Zhu and Sun 2020) demonstrated a similar trend using computational fluid dynamics (CFD) simulations of fruit fly forward flight. Results showed that as a fruit fly's flight speed increases, its stroke plane becomes more vertical, and its wing angle of attack during the upstroke increases. In addition, a fruit fly's downstroke contributes approximately half of the total lift at low forward flying speeds, while at high forward flying speeds, the downstroke contributes almost all of the total lift. Song et al. (Song, Luo et al. 2014, Song, Tobalske et al. 2016) also performed CFD simulations of hummingbird hovering and fast forward flight. Results showed that during hummingbird hovering, lift production is asymmetric between the downstroke and upstroke, with the

downstroke producing 74% of the total lift, consistent with particle imaging velocimetry results(Warrick, Tobalske et al. 2005). During hummingbird fast forward flight, the downstroke contributes all of the total lift, and negative lift is generated during the upstroke. Song et al. suggest that at high hummingbird forward flying speeds, the upstroke is used to generate thrust at the cost of lift production.

The hawkmoth (*Manduca sexta*) is another small flying animal capable of both hovering and forward flight. Hedrick & Daniel (Hedrick and Daniel 2006) discovered many different sets of kinematic parameters capable of producing hovering flight in a model hawkmoth. Their results suggest that the flapping mechanism used in hawkmoth flight is likely determined by factors beyond kinematic and aerodynamic performance. These factors may include biological constraints, such as the ability to apply a single wingbeat pattern to several different flight modes. For a flying animal of its size, a hawkmoth's maximum forward flying speed has been reported much lower than expected. Stevenson et al. (Stevenson, Corbo et al. 1995) used the hawkmoth's body mass to calculate a theoretical maximum flying speed of 7-10 m/s. However, experimental results have shown that hawkmoths are incapable of sustaining steady forward flight at speeds greater than 5m/s (Willmott and Ellington 1997, Hedrick, Martínez-Blat et al. 2017). Studying how a hawkmoth's wing kinematics and aerodynamics change as its flight speed increases can help explain why its maximum forward flying speed is low compared to other flying animals with similar body mass, such as hummingbirds. Willmott & Ellington (Willmott and Ellington 1997) used high-speed videography to calculate a hawkmoth's wing kinematics for flight speeds ranging from 0 m/s (hovering) to 5 m/s (forward flight). Results showed that as the hawkmoth's flying speed increased, its stroke plane angle

became more vertical. This trend is consistent with the previously discussed results for other flying animals. Willmott & Ellington (Willmott and Ellington 1997) also studied the aerodynamic performance of hawkmoths flying over the same range of speeds. They used a modified blade-element (BEM) approach to calculate the mean lift and drag coefficients for stationary hawkmoth wings. Because the wings were stationary, a time history of the instantaneous lift and drag was not provided. In addition, the researchers were able to qualitatively determine that the downstroke increasingly dominates lift support as forward flying speed increases, but exact contributions were not calculated in their study.

In addition to the above experimental measurements, Aono et al. (Aono, Shyy et al. 2009) used real insect data to perform CFD simulations of hawkmoth hovering. The researchers noted the formation of a doughnut-shaped vortex ring in the wake of the hovering hawkmoth. Their results showed that the downstroke and upstroke both provided significant contributions to the total lift, but simulations for hawkmoth forward flight were not part of this study. Zheng et al. (Zheng, Hedrick et al. 2013) also used real hawkmoth hovering data to compare CFD simulation results with a BEM based approach. Results showed that the BEM approach did not match the predictive abilities of the CFD. The researchers also found that for hawkmoth hovering, most of the lift is generated during the downstroke, similar to results from hummingbirds. This study also did not include any simulations of hawkmoth forward flight. Yao & Yeo (Yao and Yeo 2020) performed CFD simulations of both hawkmoth hovering and forward flight. However, wing kinematics were prescribed using a generic proportional-integral-derivative (PID) controller and were not based on real hawkmoth flapping data. Results from this study showed that for hawkmoth hovering, the downstroke and upstroke provided approximately equal

contributions to the total lift generated during each wingbeat. At a forward flying speed of 1.3 m/s, the downstroke provided most of the lift, but positive lift was still generated during the upstroke. At all flight speeds greater than 1.3 m/s, the upstroke generated negative lift. Yao & Yeo suggest that this trend is due to the highly vertical stroke plane at high forward flying speeds.

As described above, prior experimental measurements and computational simulations of hawkmoth flight have mainly focused on hovering. The exception, Yao & Yeo (Yao and Yeo 2020), performed CFD simulations of hawkmoth forward flight, but used a flat-plate wing with flapping kinematics prescribed as sinusoidal equations. The present study is among the first to use real hawkmoth flight data to simulate hawkmoth flight over a range of flying speeds. We aim to find out what prevents the hawkmoth from achieving a fast forward flying from a fluid dynamics perspective. In the current study, hawkmoth wing kinematics were reconstructed based on high-speed video recordings of flying hawkmoths at speeds of 0 m/s, 2 m/s, and 4 m/s in a wind tunnel. The reconstructed hawkmoth model was then simulated using an in-house immersed boundary method (IBM) based in-house CFD solver. Simulation results were used to calculate instantaneous lift and drag forces produced by the flying hawkmoth, and power consumptions required to achieve different flight motion. The force generation on the deformable wing surfaces and its associated near and far wake structures were compared across different flying speeds.

1.2 Hydrodynamics of Metachronal Swimming

Metachronal rowing is a biological propulsion mechanism employed by many swimming invertebrates. Animals that locomote via this mechanism feature rows of

appendages that oscillate in a coordinated wave. This metachronal wave is induced by a constant phase lag between adjacent appendages, and it propagates through the row as appendages oscillate. The beat cycle of a rowing appendage consists of a power stroke and a recovery stroke. During the power stroke, the appendage remains straight and sweeps in the direction opposite to the body's motion; during the recovery stroke, it bends and returns to its original position (Sleigh 1976). The power stroke generates thrust, while the recovery stroke generates a small amount of drag.

Previous studies have suggested that metachronal coordination of appendages enhances hydrodynamic performance. Barlow et al. (Barlow, Sleigh et al. 1993) used particle image velocimetry (PIV) to investigate a swimming ctenophore, and they concluded that flow interactions between adjacent metachronal appendages improve mechanical efficiency. Other studies have examined the effects of varying the phase lag between appendages. Alben et al. (Alben, Spears et al. 2010) compared a krill's metachronal kinematics with synchronous kinematics, in which the phase lag is zero. They observed that metachronal rowing results in a higher average body speed. Ford and Santhanakrishnan (Ford and Santhanakrishnan 2021) reached a similar conclusion using PIV of a robotic krill. They also noticed that when a phase lag is introduced, the robotic krill's body velocity decreases as appendages move toward each other and increases as they move apart. This suggests that the performance benefits of metachronal rowing are due to appendage tip vortex interactions. Throughout one beat cycle, an appendage generates positive and negative tip vortices that contribute to thrust generation (Kim and Gharib 2011). As appendages beat in a metachronal wave, tip vortices interact in various ways that influence hydrodynamic performance. In general, vortex interactions may be

characterized as either constructive or destructive (Gopalkrishnan, Triantafyllou et al. 1994). Vortices are strengthened by constructive interactions, and they are weakened or destroyed by destructive interactions. Only a few previous studies have examined the tip vortex interactions that occur during metachronal rowing. Dauptain et al. (Dauptain, Favier et al. 2008) ran numerical simulations of ctenophore swimming in which they artificially increased the distance between adjacent appendages, thereby reducing vortex interactions. Their results showed that as the distance increases, efficiency (equal to thrust divided by power output) decreases. This observation supports the hypothesis that tip vortex interactions contribute to hydrodynamic performance. In another study, Ford and Santhanakrishnan (Ford and Santhanakrishnan 2021) increased the distance between appendages of a robotic krill. Their PIV results showed that the counterrotating vortices produced by appendage power strokes and recovery strokes interact throughout the beat cycle. The authors concluded that these vortex interactions are the source of thrust augmentation observed during metachronal rowing. However, it is unknown whether this thrust augmentation mechanism is consistent across all body shapes and scales.

Tip vortex dynamics are highly dependent on the Reynolds number. Kim and Gharib (Kim and Gharib 2011) showed that at low *Re* (≈10), tip vortices remain attached to an appendage throughout its beat cycle. However, as *Re* increases and inertial forces increasingly dominate, tip vortices tend to separate from the beating appendages. Because these vortices contribute to thrust generation, increasing *Re* impacts the hydrodynamic performance of metachronal rowing. In nature, metachronal rowing is found in a wide variety of species, ranging in size from paramecia (*Re* = 0.2) (Zhang, Jana et al. 2015) to lobsters (*Re* = 7500) (Lim and DeMont 2009). Among these species are ctenophores (*Re* =

10-200), which are the largest animals that locomote via ciliary propulsion (Matsumoto 1991). Ctenophores are lined by eight rows of appendages called ctenes, and each ctene consists of thousands of cilia fused together (Afzelius 1961). Most previous studies on ciliary hydrodynamics have assumed that flow is dominated by viscous effects ($Re < 1$). However, due to their size, ctenophores are ideal candidates for studying how cilia function in the presence of inertial forces. Several previous studies have explored the relationship between *Re* and ctenophore hydrodynamic performance. Barlow et al. (Barlow, Sleigh et al. 1993) increased *Re* for a swimming ctenophore by adjusting its ctene beating frequency. They found that as *Re* increases, high-speed flow separates from the ctene tip and is shed into the flow stream. In a separate study, Herrera-Amaya et al. (Herrera-Amaya, Seber et al. 2021) examined how varying *Re* affects the spatiotemporal asymmetry of ctene kinematics. Their results showed that increasing *Re* results in a quicker power stroke and slower recovery stroke. They also concluded that in time-reversible flow conditions (low *Re*), the power stroke and recovery stroke must be spatially asymmetric to generate thrust, while at higher *Re*, this asymmetry becomes less pronounced. These findings indicate that varying *Re* strongly influences ctene kinematics and hydrodynamic performance. However, it is unclear how *Re* affects the interciliary flow interactions that occur during ctenophore swimming.

Apart from their cilia, ctenophores are also noteworthy for their diverse body morphologies. Depending on the species, ctenophores may possess lobate, tentacled, oblong, or roughly spherical bodies (Tamm 2014). Despite this natural diversity of body shapes, previous studies on ciliary hydrodynamics have largely assumed the ciliated

substrate is completely flat. It is therefore unknown how substrate curvature impacts the hydrodynamic performance of metachronal rowing.

To address these gaps in knowledge, the present study employs an in-house immersed-boundary-method-based computational fluid dynamics (CFD) solver to simulate metachronal rowing. We used a high-speed video of a swimming ctenophore to reconstruct three-dimensional ctene rowing kinematics, and the reconstruction was simulated within the in-house solver. Simulation results were used to calculate force generation and power consumption for each ctene, as well as vorticity and wake structures for the entire row. Using these results, we aim to answer three questions: (i) how ctene tip vortex interactions improve hydrodynamic performance, (ii) how varying *Re* affects interciliary interactions, and (iii) how varying substrate curvature affects ctene row hydrodynamics.

1.3 Organization of Thesis

Chapter 2 describes the methodology employed in this study. A brief explanation of the numerical method is provided. Then, hawkmoth flight reconstruction and simulation setup are described. Ctenophore swimming reconstruction and simulation setup are also described. Chapter 3 examines the aerodynamic performance of hawkmoth flight. Flapping wing kinematics and force generation are examined across a range of forward flying speeds. Chapter 4 explores the hydrodynamic performance of ctenophore swimming. The effects of interciliary hydrodynamic interactions are described. The effects of varying the Reynolds number and substrate curvature are also examined. Chapter 5 summarizes the main findings of this study and presents recommendations for future research.

Chapter 2: Methodology

2.1 Governing Equations and Numerical Method

The numerical methodology of the immersed-boundary-method-based in-house CFD solver employed in the current study is briefly introduced here. The 3D viscous, incompressible Navier-Stokes equations can be written in a tensor form as follows:

$$\frac{\partial u_i}{\partial x_i} = 0;\ \frac{\partial u_i}{\partial t} + \frac{\partial (u_i u_j)}{\partial x_j} = -\frac{\partial p}{\partial x_i} + \frac{1}{Re}\frac{\partial}{\partial x_j}(\frac{\partial u_i}{\partial x_j}) \tag{1}$$

where u_i are the velocity components, p is the pressure, and Re is the Reynolds number.

The above equations are discretized using a cell-centered, collocated arrangement of the primitive variables, and are solved using a finite difference-based Cartesian grid immersed-boundary method (Mittal, Dong et al. 2008). The equations are integrated in time using the fractional step method. A second-order central difference scheme is employed in space discretization. The Eulerian form of the Navier-Stokes equations is discretized on a Cartesian mesh and boundary conditions on the immersed boundary are imposed through a ghost-cell procedure. This method has been successfully applied in the simulations of insect flights (Li, Dong et al. 2018, Li, Dong et al. 2020, Li 2021) and bio-inspired propulsions (Li and Dong 2016, Li, Wang et al. 2019, Li, Dong et al. 2020, Lei, Crimaldi et al. 2021). Validations of the current in-house CFD solver can be found in previous studies (Li, Dong et al. 2015, Li and Dong 2017, Li, Jiang et al. 2017, Lei and Li 2020).

2.2 Hawkmoth Flight

Before hawkmoth flight was simulated, hawkmoth flight kinematics were recorded using a high-speed camera setup. The high-speed recordings were then used to reconstruct flight motions across a range of forward-flying speeds. Following reconstruction, the model hawkmoth was simulated within the in-house CFD solver. Solver results were validated using previous studies on hawkmoth hovering. These procedures are described in detail below.

2.2.1 Experimental Setup and Filming Procedures

Hawkmoths were recorded flying at three different flight speeds- hovering (0 m/s), slow forward flight (2 m/s), and fast forward flight (4 m/s). Moths were males acquired as pupae from the domestic colony at the University of North Carolina at Chapel Hill Department of Biology. Following eclosure, moths were placed in individual 30×30×30 cm mesh cages in an environmental chamber maintaining ~25°C and a 20:4 L:D cycle. Before filming, moths were not fed for a minimum of 12 hours. At recording, each moth was placed inside a wind tunnel (octagonal working section, 1.2m long and 0.6m diameter, see Ortega-Jimenez et al. (Ortega-Jimenez, Greeter et al. 2013) for further details, and an artificial flower with a 1:4 honey: water mix was provided for the insect to feed on; moths were trained via prior experience to recognize the flower and feed from it at a variety of tunnel flow speeds. Three high-speed cameras (two Phantom v7.1 equipped with 35mm Nikon lenses, and one Phantom v5.1 with a Zeiss 50mm lens, Vision Research Inc., Wayne, NJ, USA) operating at 1000 frames s^{-1} with a 300 μs shutter duration were used to record hawkmoth flight. Illumination for the cameras was provided by four 12 W multi-LED infrared (730 nm) lights (Larson Electronics LLC, Kemp, TX, USA); these emit at a

wavelength below the hawkmoth visual spectrum and thus do not alter flight behavior. The cameras were calibrated for 3D kinematics using a structure-from-motion approach (Theriault, Fuller et al. 2014). Recordings from a single individual collected from a single flight bout collected by changing wind tunnel speeds without removing the animal were selected for detailed 3D reconstruction and meshing for computational simulation. The morphological data for the hawkmoth used in this study is summarized in Table 1. Note that the moth was allowed to hover and feed to satiation after the video data were collected, and the pre-feeding mass from Table 1 is expected to be characteristic of the moth during recordings. The flight speeds were recorded in the following order: 2 m/s, 4 m/s, and 0 m/s.

Table 1. Morphological data for the hawkmoth in this study. Wing data is for a single side wing combining both forewing and hindwing.

Parameter	Values
Body mass before feeding (g)	1.45
Body mass after feeding (g)	1.95
Body length (cm)	5.3
Wing mass (g)	0.0382
Wing span length, R (cm)	5.5
Mean wing chord, c (cm)	2.3
Wing area, S (cm^2)	10.7
Flapping frequency, f (Hz)	27.9 ± 2.4

2.2.2 Reconstruction of Flapping Kinematics

After recording hawkmoth hovering (0 m/s), 2 m/s forward flight, and 4 m/s forward flight, a meshed model of the flying hawkmoth was reconstructed using Autodesk Maya. The model was superimposed over side-view and top-view high-speed video recordings of hawkmoth flight. For each flying speed, one flapping cycle was selected where the hawkmoth body was relatively stationary. At various points throughout the selected wingbeat cycle, the morphology of the model hawkmoth's left wing was adjusted to align with the high-speed recording. Between these points, linear interpolation was used to reconstruct hawkmoth flapping motions. Then, the flapping left wing was mirrored across the hawkmoth's body to complete the reconstruction. Figure 1 shows a comparison of the hawkmoth model template used for reconstruction with an image of a real hawkmoth.

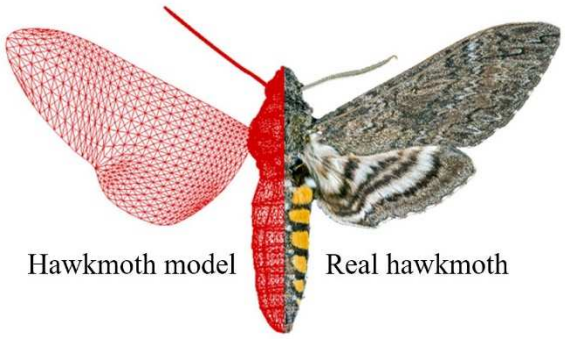

Figure 1. Comparison between hawkmoth meshed model and real hawkmoth.

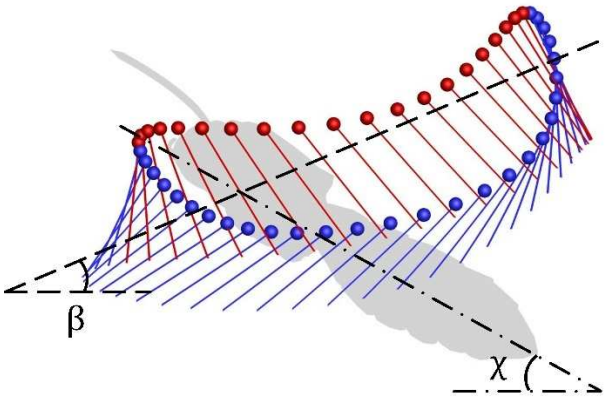

Figure 2. Definition of stroke plane angle (β) and body incline angle (χ).

Using the reconstructed kinematics, the hawkmoth's body incline angle (χ) and stroke plane angle (β) were determined for each flight speed. As shown in Figure 2, the body incline angle is defined as the angle between the hawkmoth body and the horizontal x-axis. The stroke plane angle is defined as the angle between the stroke plane and the x-axis. The stroke plane was determined based on the least square plane of the wingtip trajectory that pass through the wing root and is represented by the dashed line in Figure 3. Next, wing kinematics were quantified on the stroke plane using three Euler angles: wing stroke (ψ **),** wing deviation **(**ϕ), and wing pitch (θ). The wing stroke angle provides the location of the wing in the stroke plane, defined as the angle between the projection of root-to-tip connection line and the z-axis. The deviation angle is the angle between the line from wing root to tip and its projection onto the stroke plane. The wing pitch angle provides the angle between the wing chord and the stroke plane.

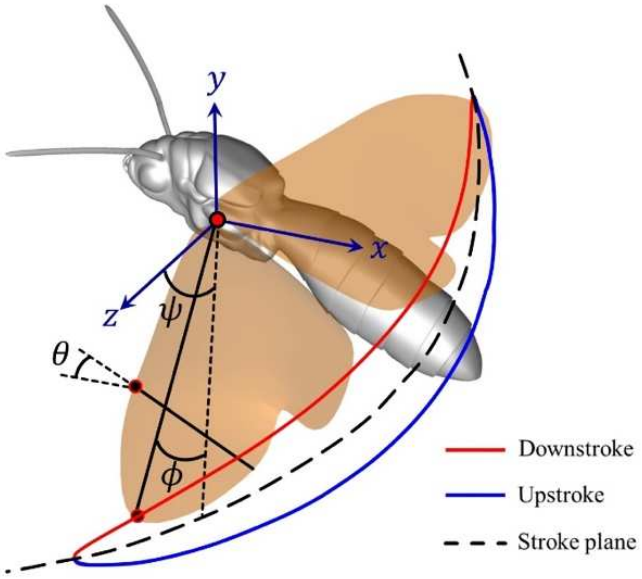

Figure 3. Wing Euler angles definition, including wing stroke (ψ), wing deviation (ϕ), and wing pitch (θ) angles.

2.2.3 Simulation Setup

Figure 4 shows the simulation setup for hawkmoth hovering and forward flight. The domain mesh has two refined layers. As seen in this figure, a very high-resolution mesh is provided in a rectangular region around the hawkmoth. Around this region, there is a secondary denser mesh, and beyond this layer, the grid is stretched rapidly. Different computational grids were used for hovering and forward flight to accommodate different relative positions of downwash. In addition, different boundary conditions were also applied to the two meshes. For hovering, a zero velocity gradient was used for all boundaries. For forward flight, the inflow boundary condition was specified at the front of the fluid domain, while an outflow boundary condition was used at the back of fluid domain. At all other boundaries, a zero gradient was adopted. The forward flight grid contains

approximately 1 million more computational cells than the grid used for hovering flight. In order to achieve a periodic state of the force history, all simulations were run for four flapping cycles. The hawkmoth simulation results we present in the results section is based on the fourth flapping cycle.

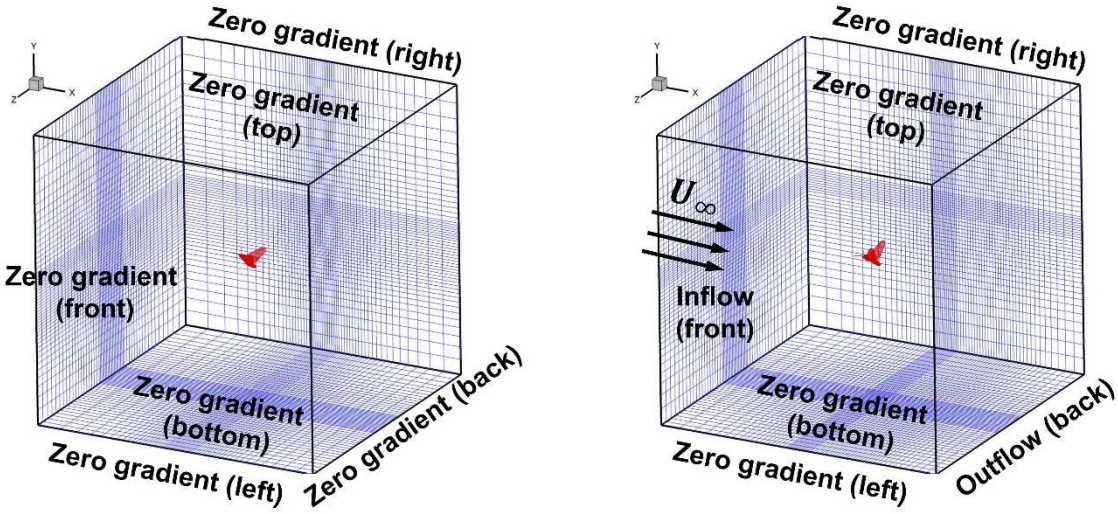

Figure 4. Simulation setup and computational grids applied in the study. Grids are shown for hovering (left) and forward flight (right).

The simulations were carried out on a non-uniform Cartesian grid. The grid size employed in the current simulations is 225×193×225 for hovering and 313×153×225 for forward flight. To ensure the simulation results are grid-independent, grid independence studies were performed for both hovering flight and forward flight at 4 m/s. Figure 5 shows the comparison of simulated lift and drag for a single hawkmoth wing in three grids of different densities at hovering. For both lift and drag, the difference between the cycle average force for the medium and fine meshes is less than 3%.

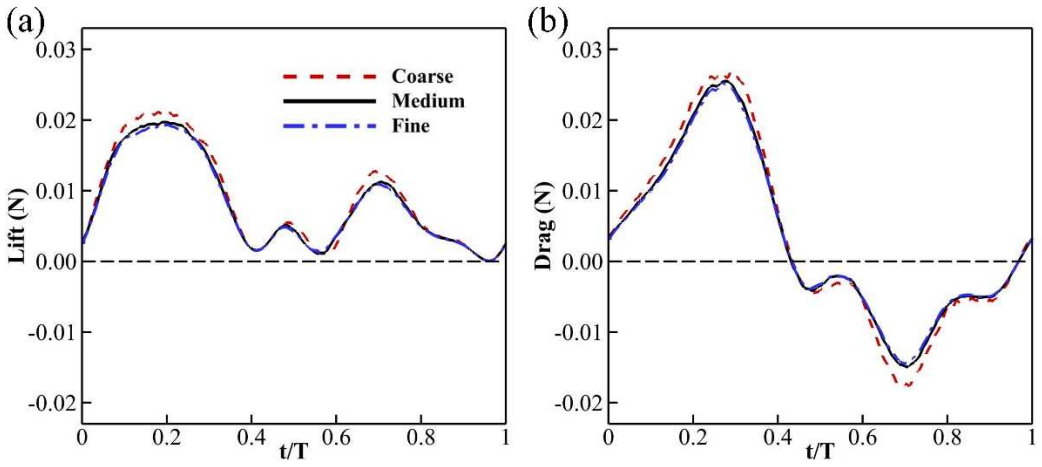

Figure 5. Lift and drag force production during hovering flight by a single hawkmoth wing. Results are shown for three different grid densities- coarse (177×145×177≈5 million), medium (225×193×225≈10 million), and fine (257×225×257≈15 million).

In the present study, we observed that the hawkmoth slightly changed its flapping frequency as the flying speed increased from 0 m/s (hovering) to 4 m/s (forward flight). In order to make a fair comparison, we incorporate both cycle-averaged wing-tip velocity and flight speed in the definition of Reynolds number. Following the previous literature (Han, Chang et al. 2016), the Reynolds number (*Re*) and advance ratio (*J*) for insect flight are defined as:

$$Re = \frac{(U_{tip,ave}+U_\infty)c}{v} = \frac{(1+J)(2\Phi fR)}{v} \quad (2)$$

$$J = \frac{U_\infty}{U_{tip,ave}} = \frac{U_\infty}{2\Phi fR} \quad (3)$$

where U_∞ represents the body moving velocity (zero for the hovering case); $U_{tip,ave}$ is the mean wing tip velocity and can be expressed as $2\Phi fR$, in which Φ is the stroke amplitude,

f is the flapping frequency, and R is the wing root to tip length (0.055m for all cases); c is the average wing chord length (0.023m for all cases); and v is the fluid kinematic viscosity (around 1.56×10^{-5} m^2s^{-1} for air at room temperature of 25℃).

To evaluate the aerodynamic performance of hawkmoth flight, the surface pressure and shear stresses along the wing surfaces were obtained by solving the Navier-Stokes equations. The lift (F_L, along the vertical direction) and drag (F_D, along the horizontal direction) forces are presented as non-dimensional coefficients, which are computed by $C_L = F_L/0.5\rho U_{tip,ave}^2 S$ and $C_D = F_D/0.5\rho U_{tip,ave}^2 S$. Here, C_L and C_D represent the lift and drag coefficients, $U_{tip,ave}$ is the cycle-averaged wing tip velocity, and S denotes the area of the wing surface.

2.2.4 Validation of Computational Modelling

To validate the CFD solver used in this study, the aerodynamic force production of the hovering hawkmoth was compared to previous studies. Aerodynamic lift and drag production were calculated for both wings and the hawkmoth's body. Figure 6 compares our CFD results with the forces calculated by Zheng et al. (Zheng, Hedrick et al. 2013) using both numerical and experimental approaches. Numerical results obtained by Aono et al. (Aono, Shyy et al. 2009) are also included. As illustrated in Figure 6, the force magnitudes and overall trend of our calculations are consistent with the literature. Specifically, the force predictions from the current study are aligned best with the experimental estimation of aerodynamic forces calculated in Zheng's study (Zheng, Hedrick et al. 2013). Slight variations in force magnitude and phase lag can be explained by the fact that different hawkmoths were used in each study.

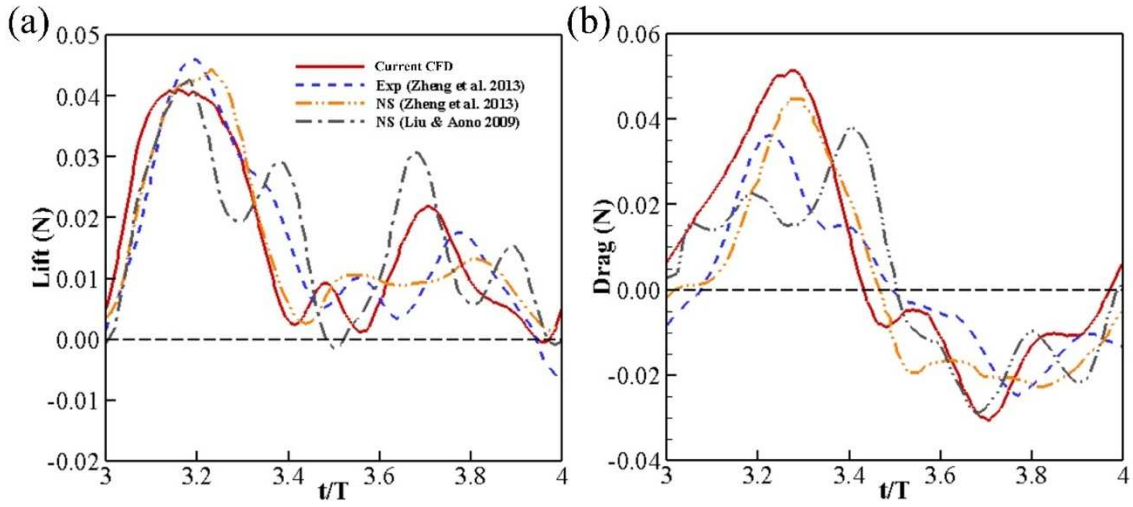

Figure 6. Validation of the in-house CFD solver used in this study. Lift and drag forces produced by a hawkmoth's wings and body in hovering flight are plotted against previous experimentally and computationally determined results. Experimental and numerical results obtained by Zheng et al. (Zheng, Hedrick et al. 2013) and Aono et al. (Aono, Shyy et al. 2009) are included.

2.3.5 Evaluation of Power Consumption

To determine the total power required for hawkmoth flight, the mechanical power (P_{mech}) was calculated using a similar treatment as presented by Wan et al. (Wan, Dong et al. 2015). The mechanical power includes two components, namely, aerodynamic power (P_{aero}) and inertial power (P_{iner}). Specifically, the aerodynamic power is the power needed to overcome air resistance, and it is defined as the surface integral of the product of the pressure and velocity of each element (Eq. 4). The area of each element is ds, and the unit vector normal to the surface is **n**.

$$P_{aero} = -\iint p\boldsymbol{n} \cdot \boldsymbol{u}_c ds \tag{4}$$

$$P_{iner} = \iint \bar{\rho}_w \bar{h} \frac{d\boldsymbol{u}_c}{dt} \cdot \boldsymbol{u}_c ds \tag{5}$$

The inertial power is the power needed to accelerate each wing, and it is defined as the surface integral of the product of the average wing density, average wing thickness, acceleration of each element, and the velocity of each element (Eq. 5). The mechanical power required to move each wing is the sum of the aerodynamic power and the inertial power (Eq. 6). The power can be normalized by dividing by the body mass (m_b) of the hawkmoth to compute the mass-specific power (Eq. 7).

$$P_{mech} = P_{aero} + P_{iner} \tag{6}$$

$$P^* = \frac{P_{mech}}{m_b} \tag{7}$$

The true cycle-averaged mechanical power $\bar{P}^*$ depends on the elastic energy storage of the hawkmoth wings and therefore cannot be reported directly. Instead, limiting cases representing 0% and 100% elastic storage must be considered, and the real $\bar{P}^*$ lies between these values (Lyu and Sun 2021). In the case of 0% elastic storage, all negative power is dissipated, and the cycle-averaged mechanical power can be written as

$$\bar{P}^*_{mech,0\%} = \bar{P}^+ \tag{8}$$

In the case of 100% elastic storage, all negative power is stored for later use, and the cycle-averaged mechanical power can be written as

$$\bar{P}^*_{mech,100\%} = \bar{P}^+ - |\bar{P}^-| \tag{9}$$

2.3 Ctenophore Swimming

Before ctenophore swimming was simulated, ctene kinematics were recorded using a high-speed camera setup. The high-speed recording was then used to create a 3-D meshed reconstruction of a single ctene row. Following reconstruction, the meshed row was simulated within the in-house CFD solver. These procedures are described in detail below.

2.3.1 Reconstruction of Ctene Kinematics

To capture real ctene kinematics, a forward-swimming ctenophore was recorded at 1000 frames per second with a shutter speed of 900μs. The camera setup for this recording is described in detail by Amaya-Herrera et al. (Herrera-Amaya, Seber et al. 2021). The high-speed video was imported into Autodesk Maya, where it was used to create a meshed model of a single ctene row. The model row, shown in Figure 7, consists of sixteen rectangular ctenes situated along a curved rectangular substrate. As observed in the real ctenophore, larger ctene meshes are located near the middle of the row. In addition, the substrate curvature matches the real ctenophore's body curvature. To reconstruct swimming kinematics, the model ctenes were aligned with different frames of the high-speed video. Their motions were linearly interpolated between these frames to complete one full beat cycle. The baseline reconstruction created using this method was modified throughout this study by removing certain ctenes and adjusting the substrate curvature. Figure 8. compares the reconstruction with images of the real ctenophore. Both the reconstruction and the real ctenophore exhibit a metachronal wave that travels through ctene row as the beat cycle progresses.

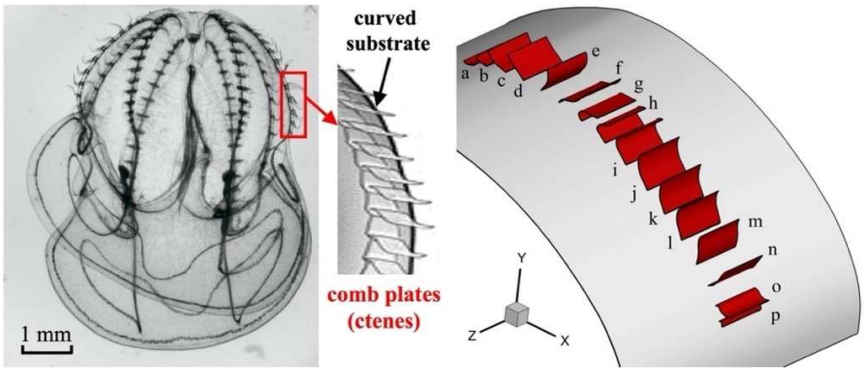

Figure 7. Comparison of a real ctenophore body with the reconstruction. The image on the left shows eight ctene rows arranged symmetrically around a ctenophore's body. Each row consists of sixteen ctenes situated along a curved substrate. The reconstructed model ctene row is shown on the right. The curved body substrate is colored gray, and the sixteen ctenes are colored red and are labelled alphabetically.

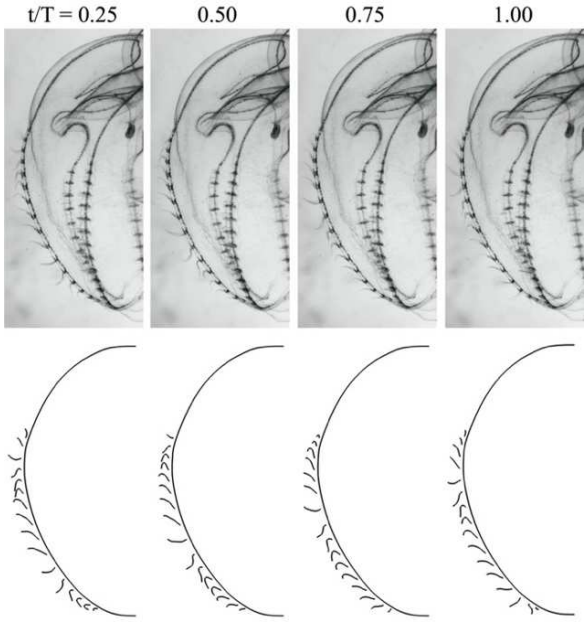

Figure 8. Time sequence of a metachronal wave propagating through the real ctene row (top) as well as the row reconstruction (bottom). The wave begins at the bottom of the row and travels toward the top as the beat cycle progresses.

The ctenophore used in this study is described by several morphological and kinematic parameters. These parameters include body length (L_b), body curvature (κ), body velocity (U_b), average ctene length (l), phase lag (P_L), stroke amplitude (Φ), ctene beat frequency (f), and ctene tip velocity (U_{tip}). Body curvature is defined as $1/R$, where R is the radius of the curved substrate. The phase lag is defined as the time delay between the beat cycles of adjacent ctenes and is expressed as a percentage of the overall cycle time. The stroke amplitude is defined as the angle traced by the ctene tip during the power stroke. Body length (L_b), ctene length (l), and stroke amplitude (Φ) are labelled in Figure 9. Ctene tip velocity is computed by $U_{tip} = \sqrt{u_{tip}^2 + v_{tip}^2 + w_{tip}^2}$, where u_{tip}, v_{tip}, and w_{tip} are ctene tip velocity components in the x, y, and z directions, respectively. The mean tip velocity $\overline{U_{tip}}$ is determined by averaging the tip velocities of the middle eight ctenes (e-l).

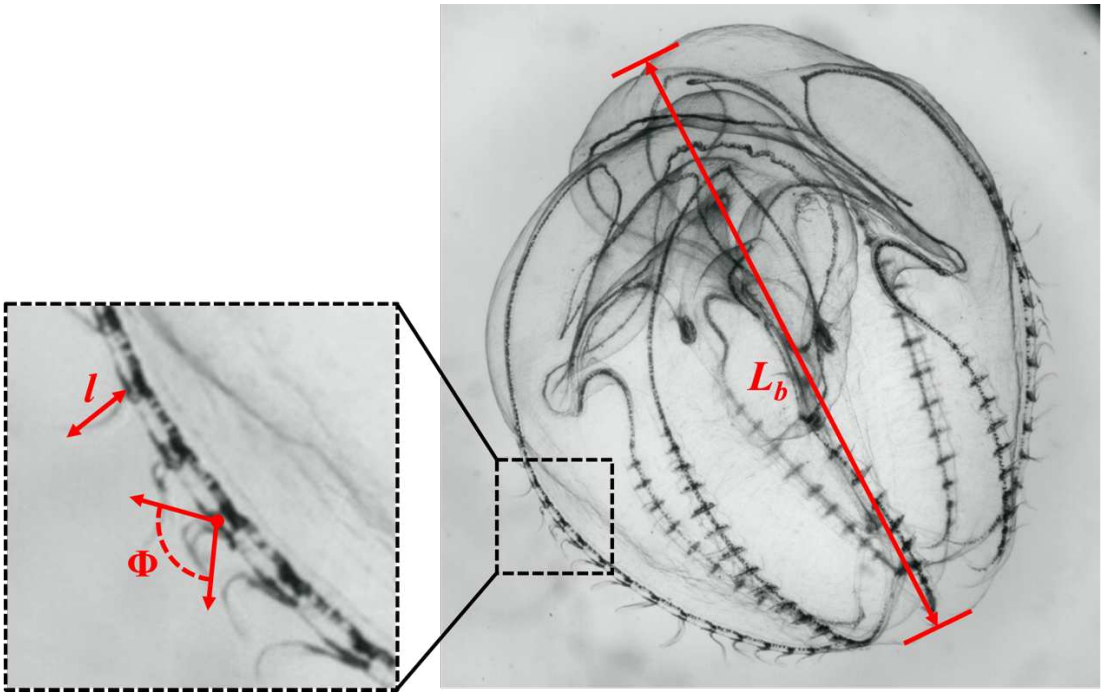

Figure 9. Diagram showing ctenophore body length (L_b), ctene length (l), and stroke amplitude (Φ).

2.3.2 Simulation Setup

Figure 10 shows a schematic of the computational grid and boundary conditions employed in this study. The meshed ctene row was situated at the bottom a non-uniform Cartesian computational grid that contained two defined layers. The ctene row was located within a very high-density region, and this region was surrounded by a secondary dense layer. Beyond this secondary layer, the grid was stretched rapidly. A constant velocity inflow was specified at the front of the fluid domain, and an outflow boundary condition was applied at the back of the domain. All remaining boundaries were assigned a zero-gradient boundary condition. To achieve a state of periodic flow, simulations were run for four ctene beat cycles. Results presented in this paper are based on the fourth cycle.

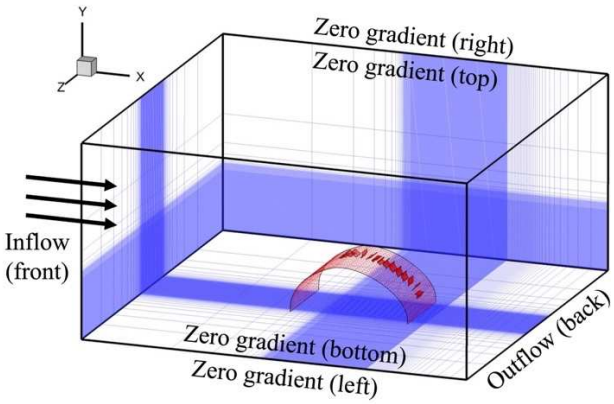

Figure 10. Schematic of the computational grid and boundary conditions used in this study. The computational grid size is 352×210×114, and the meshed model ctene row contains approximately 7000 triangle elements.

As a ctenophore swims, the flow around its body differs from the oscillatory flow produced by each individual ctene. To account for this difference, two Reynolds numbers are defined. The body Reynolds number (Re_b) describes the flow around a ctenophore's body as it swims in a particular direction. Following the previous literature (Herrera-Amaya, Seber et al. 2021), the oscillatory Reynold number (Re_ω) is used to describe flow around each ctene. These parameters are defined as:

$$Re_b = \frac{U_b L_b}{\nu} \tag{10}$$

$$Re_\omega = \frac{2\pi f l^2}{\nu} \tag{11}$$

where ν is the kinematic viscosity of seawater (ν = 1.05 mm^2/s). In this study, Re_b = 80.87 and Re_ω = 30.00.

To evaluate the hydrodynamic performance of ctenophore swimming, the surface pressure and shear stresses along the ctene surfaces were obtained by solving the Navier-Stokes equations. The lift (F_L, along the vertical direction) and thrust (F_T, along the horizontal direction) forces are presented as non-dimensional coefficients, which are computed by $C_L = F_L/0.5\rho U_{tip,ave}^2 S$ and $C_T = F_T/0.5\rho U_{tip,ave}^2 S$. Here, C_L and C_T represent the lift and thrust coefficients, $U_{tip,ave}$ is the cycle-averaged ctene tip velocity, and S denotes the area of the ctene surface. C_L and C_T are used to calculate C_F, the total force coefficient.

The instantaneous hydrodynamic power (P_{hydro}) is the power needed to overcome water resistance and was calculated as the inner product of the velocity and the hydrodynamic force. This method of computing the hydrodynamic power follows the same

definition used to evaluate the power in cicada flight (Wan, Dong et al. 2015) and fruit fly flight (Aono, Liang et al. 2008). The hydrodynamic power coefficient is calculated as $C_{PW} = P_{hydro}/0.5\rho U_{tip,ave}^3 S$.

Chapter 3: Hawkmoth Flight

In this chapter, hawkmoth wing kinematics and aerodynamic performance are compared across multiple forward flying speeds. These results help demonstrate what constrains high-speed flight in hawkmoth-like flapping-wing insects.

3.1 Flight Kinematics for Different Flying Motions

Figure 11 shows image sequences we collected in the experiments for the hawkmoth under hovering motion, 2 m/s forward flight, and 4 m/s forward flight over the course of one wingbeat cycle. Based on these images, it is clear that the hawkmoth's flight kinematics change substantially as the insect transitions from hovering to forward flight. During the hovering downstroke (approx. t/T=0.125 to 0.5), the wings sweep horizontally past the body lateral center towards the front of the moth. This 'back-and-forth' flapping behavior indicates a significant negative stroke angle as the hawkmoth begins the upstroke (t/T=0.5), as defined in Figure 3. At forward flying speeds, the hawkmoth transitions to a more 'up-and-down' flapping motion. At 4 m/s forward flight, the wings do not reach to the body lateral center at all, resulting in a consistently positive stroke angle. In addition, during hovering flight, the hawkmoth's wings exhibit a significant pitching motion, where they rotate to form an angle with respect to the stroke plane, as defined in Figure 3. The wing pitch during hovering flight is most clearly seen at t/T=0.5 and 0.625 in Figure 11. At higher flight speeds, however, the wing pitching motion is less pronounced, with the wings remaining more horizontal throughout the flapping cycle. The hawkmoth's body angle also changes as its flight speed increases. At hovering, the body angle is significantly

greater than during forward flight. In addition, Figure 11 shows that at each flying speed, the upstroke begins roughly halfway through the flapping cycle.

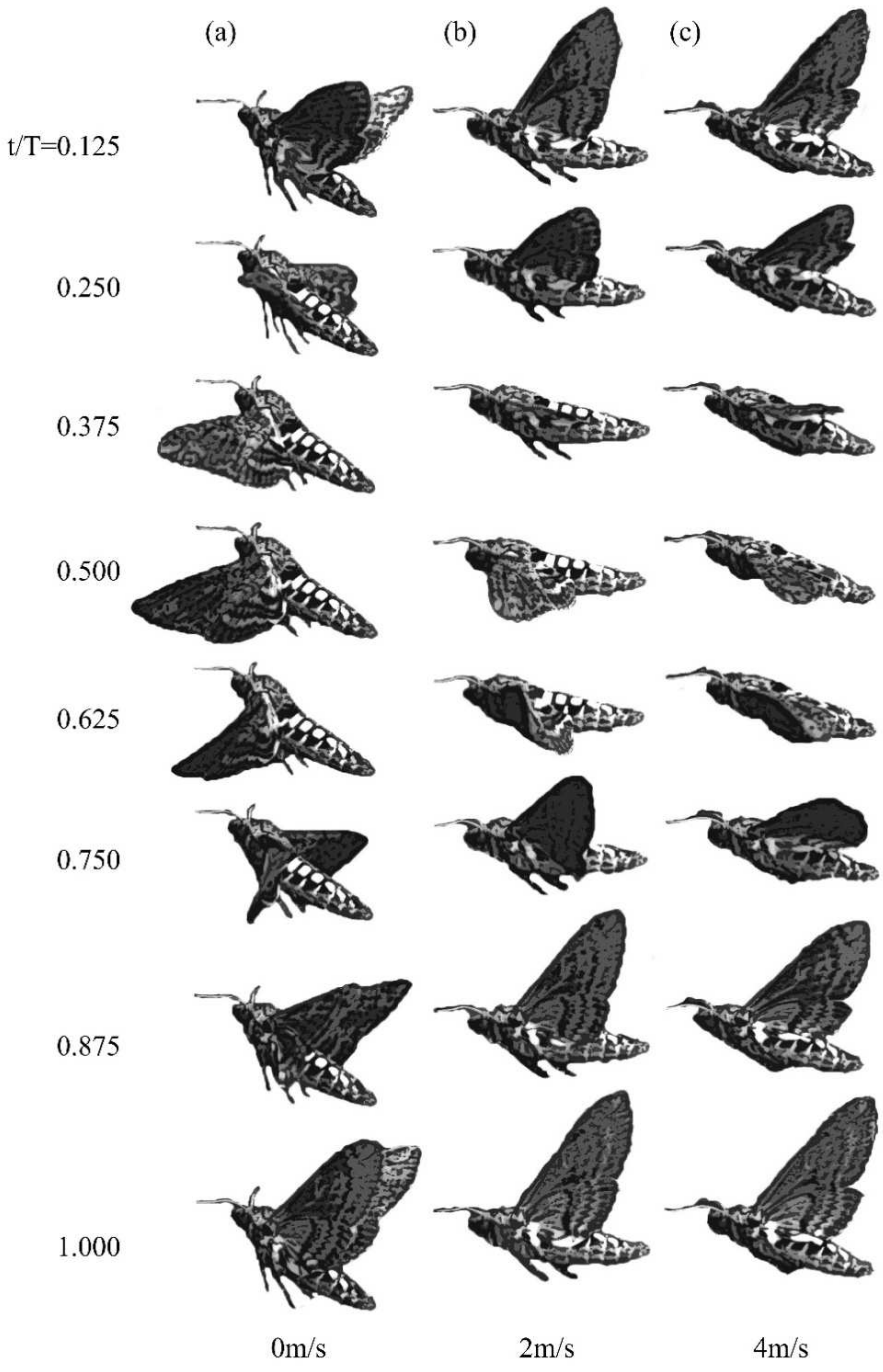

Figure 11. Images of the hawkmoth while (a) hovering and at forward flight speeds of (b) 2 m/s and (c) 4 m/s.

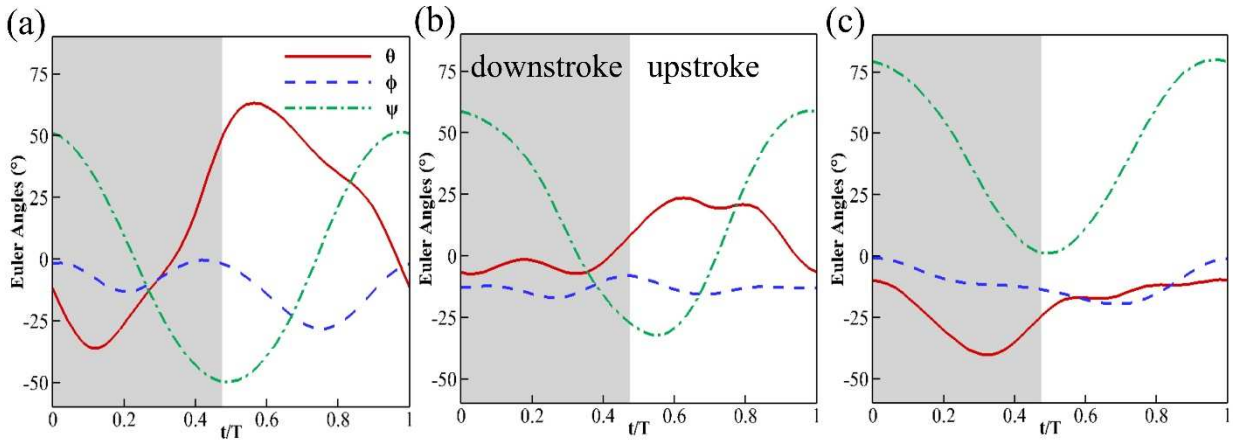

Figure 12. Wing Euler angles for (a) hawkmoth hovering, (b) 2 m/s forward flight, and (c) 4 m/s forward flight. The three Euler angles include the wing stroke (ψ), wing deviation (ϕ), and wing pitch (θ) angles.

The Euler angle plots in Figure 12 reinforce the qualitative observations made using Figure 11. At hovering, the stroke angle ψ ranges from 50° at the beginning of the downstroke to -50° at the beginning of the upstroke. This is evidence of the back-and-forth sweeping flight pattern depicted in Figure 11. At 4 m/s forward flight, the stroke angle is consistently positive. This corresponds to the transition towards a more up-and-down flapping motion at higher flight speeds. Figure 12 also shows that the wing pitch angle tends to peak during the upstroke, and as flying speed increases, the maximum pitching angle decreases. The maximum wing pitch angle decreases from 63° at hovering to -10° at 4 m/s forward flight. This is evidence of the decrease in wing pitching motion observed using Figure 11.

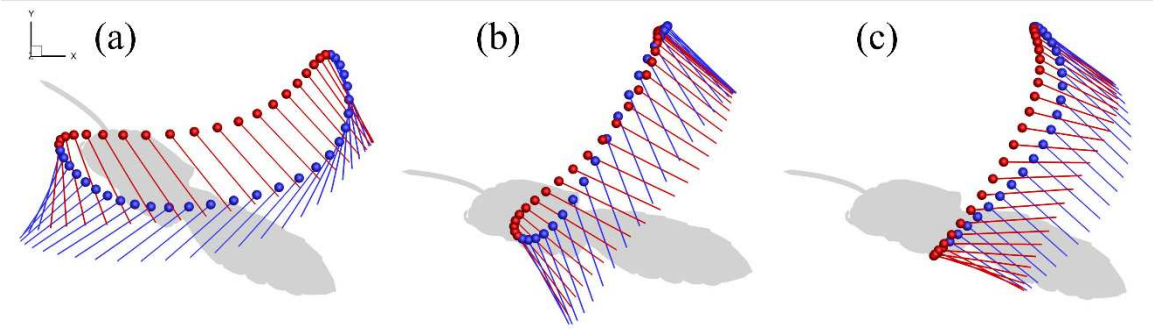

Figure 13. Wing chord trajectory for (a) hawkmoth hovering, (b) 2 m/s forward flight, and (c) 4 m/s forward flight. Colored circles in the figure denote the wing leading edge, and the lines present the wing chord at 0.75R along the wingspan. The hawkmoth flapping motion follows a counterclockwise trajectory. The downstroke is pictured in red, and the upstroke is shown in blue.

Figure 13 shows the hawkmoth's wing trajectory and wing chord orientation for hovering, 2 m/s forward flight, and 4 m/s forward flight. During hovering flight, the wing chords are significantly more vertical than during 4 m/s forward flight. This is evidence that as the hawkmoth's flight speed increases, its wing pitch angle becomes more parallel to the incoming flow, which potentially reduce the drag force generated during the downstroke. Figure 13 also shows that the stroke plane angle for hawkmoth hovering is smaller than the stroke plane angle for both forward flying speeds. In addition, the body incline angle during hovering flight is greater than during forward flight.

Table 2. Table summarizing significant wing kinematic parameters.

Parameter	Hovering	Slow Forward Flight	Fast Forward Flight
Avg. body moving velocity (U_∞)	0 m/s	2 m/s	4 m/s
Flapping frequency (*f*)	25.6 Hz	27.8 Hz	30.3 Hz
Stroke amplitude (Φ)	101.22°	91.09°	81.21°
Advance ratio (*J*)	0	0.41	0.85
Reynolds number (*Re*)	7335	10117	12863
Stroke plane angle	57.61°	72.54°	66.44°
Body incline angle	30.0°	14.0°	16.0°

Significant kinematic parameters are summarized in Table 2. Table 2 also includes the advance ratio *J* and *Re* for different flight speeds. These calculations rely on the flapping frequency *f* and the stroke amplitude Φ. The flapping frequency is equal to 25.6 Hz for hovering and increases to 27.8 Hz and 30.3 Hz for 2 m/s and 4 m/s forward flight, respectively. This increase in flapping frequency indicates that the hawkmoth must beat its wings faster to sustain level flight at higher forward flying speeds. In addition, the stroke amplitude tends to decrease as flying speed increases. This is evidence of the transition towards a more up-and-down flapping motion at higher flight speeds, as seen in Figure 11. Table 2 also shows that the stroke plane angle for both forward flying speeds is greater than for hovering, but the stroke plane angle for 2 m/s forward flight is slightly greater than

the stroke plane angle for 4m/s forward flight. In addition, the body incline angle for forward flight is significantly smaller than the body angle for hovering, but the body incline angle for 4 m/s forward flight is slightly greater than the incline angle for 2 m/s forward flight.

3.2 Evaluation of Unsteady Aerodynamics at Various Flight Speeds

Using the reconstructed body and wing kinematics described in the previous section, the unsteady flow and its associated aerodynamic forces were captured using the in-house CFD solver. In Figure 14, we compare the time history of lift and drag forces on the hawkmoth body and left wing at different flying motions. The overall trend of lift and drag forces are significantly affected by the flying speed of hawkmoth. During hovering flight (Figure 14(a)), the hawkmoth produces lift during both downstroke and upstroke, with 72% of the lift being generated during the downstroke. However, as the hawkmoth transitions to forward flight, it loses its lift-producing upstroke. At flying speeds of 2 m/s and 4 m/s, positive lift is only produced during the downstroke, and negative lift is generated during the upstroke. It is also worth noting that the lift force in the hovering case peaks three times throughout the flapping cycle: once during the downstroke, once during the transition from downstroke to upstroke, and once during the upstroke. However, during hawkmoth forward flight, the lift peaks only once at mid-downstroke (Figure 14(b-c)). For all three cases, the cycle-averaged lift generated by two wings matched reasonably well with the body weight of the hawkmoth (see Table 3). As the hawkmoth switched from hovering to forward flight, its body also generated a small amount of lift due to the wing-body interaction (Liu, Dong et al. 2016), a contribution about one order of magnitude smaller than a single wing. In addition to keeping its body aloft in the air, another challenge

for the flying hawkmoth is balancing its drag force along the horizontal direction (Figure 14(d-f)). Although the cycle-averaged drag force is close to zero for all three cases, its magnitude is significantly different at various flying speeds. During hovering flight, the hawkmoth produces a large amount of positive drag during the downstroke and negative drag (thrust) during the upstroke. As the hawkmoth's flying speed increases, the magnitude of drag production is minimized. At 2 m/s, maximum drag production is 0.012N, roughly half the maximum drag during hovering. At 4 m/s forward flight, the drag force production during both downstroke and upstroke is almost negligible. We suspect that minimizing the drag force during the entire flapping cycle is critical to achieving stable fast forward flight for the hawkmoth. By modulating its flapping kinematics to achieve this, the hawkmoth inevitably produces a large amount of negative lift during the upstroke. This biological limitation prevents the hawkmoth reaching to a higher forward flying speed as predicated based on its body size (Stevenson, Corbo et al. 1995).

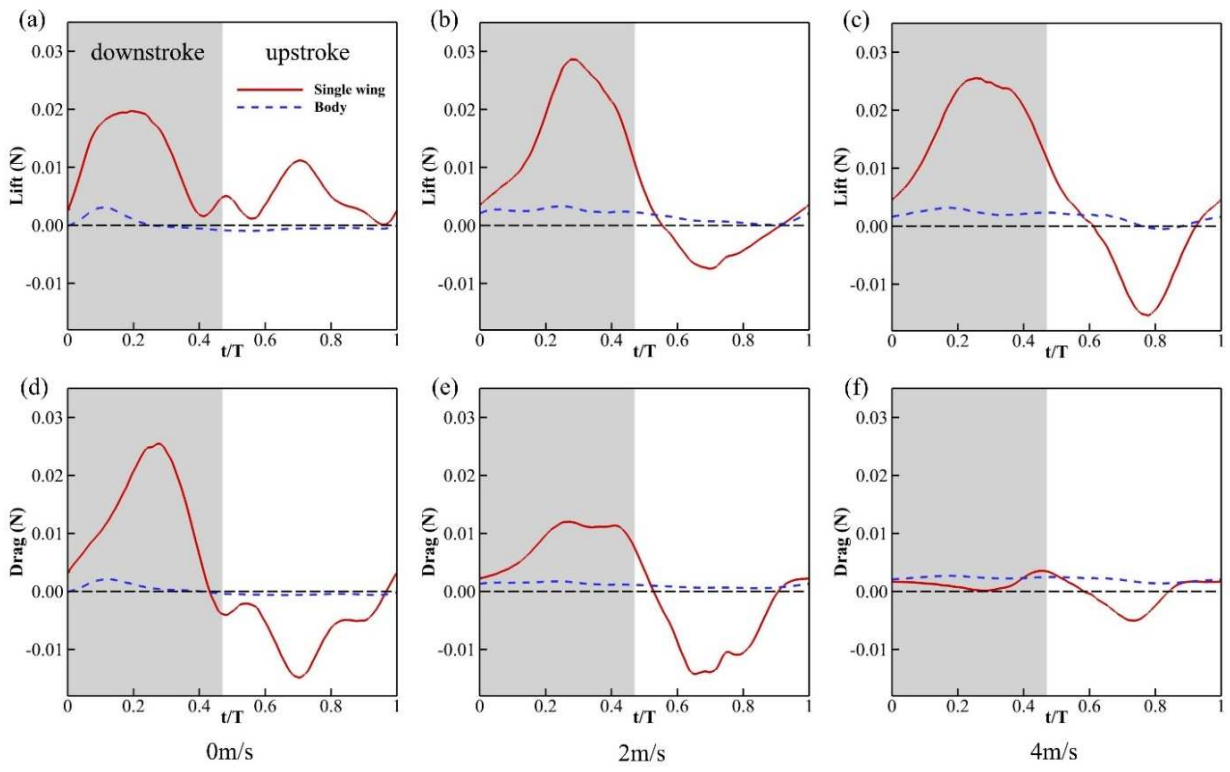

Figure 14. (a-c) Lift and (d-f) drag force production for hawkmoth hovering, 2 m/s forward flight, and 4 m/s forward flight. Force production is shown separately for a single hawkmoth wing and the hawkmoth body.

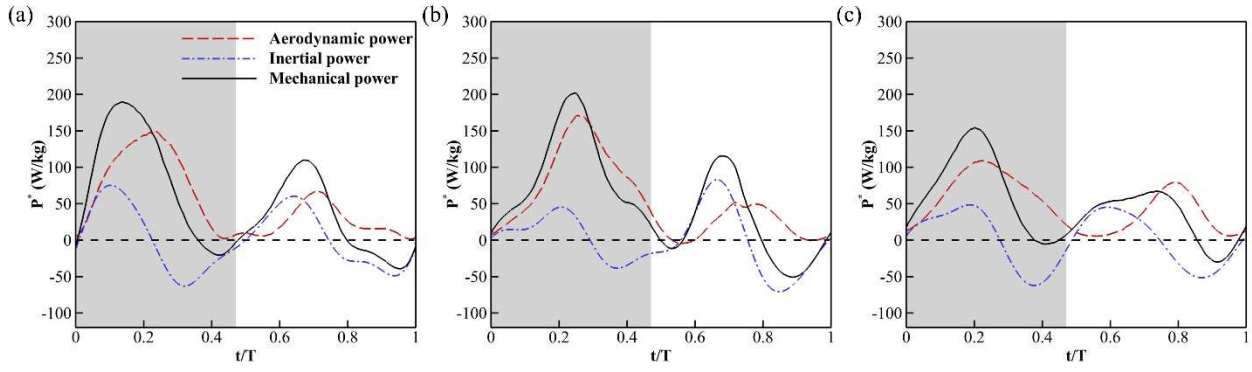

Figure 15. Instantaneous mass-specific aerodynamic, inertial, and mechanical power for (a) hovering, (b) 2 m/s forward flight, and (c) 4 m/s forward flight.

One may speculate that the flying speed limitation of hawkmoth observed in nature might be due to the high power consumption in fast flight. In order to evaluate this possibility, we calculated the instantaneous mass-specific aerodynamic, inertial, and mechanical power for hawkmoth hovering, 2 m/s forward flight, and 4 m/s forward flight, as shown in Figure 15. This figure shows that for all flight speeds, the hawkmoth consumes more aerodynamic and mechanical power during the downstroke than during the upstroke. This is consistent with results previously obtained for other insects (Wan, Dong et al. 2015, Lyu and Sun 2021). Greater power consumption during the downstroke is likely due to the downstroke's dominant role in lift production. Across all three flying speeds, most of the hawkmoth's lift is generated during the downstroke, resulting in greater power consumption. In addition, Figure 15 shows that the inertial power is positive at the beginning of each half-stroke and negative towards the end of each half-stroke. As a result, the mechanical power briefly becomes negative before each stroke reversal. This may be evidence that the hawkmoth elastically stores some negative power before beginning each stroke. Similar results were obtained by Wan et al. for the cicada (Wan, Dong et al. 2015). Table 3 reports the cycle-averaged force and power for each flight speed. Since the hawkmoth was feeding occasionally during the recordings, the cycle-averaged lift presents slight difference between different flight motions. According to our experimental measurements, the body weight of the hawkmoth was 14.2 mN before the recording, and 19.1 mN after all experiments. In addition, Table 3 also shows that the cycle-averaged mechanical power for hovering and 2 m/s forward flight is greater than for 4 m/s forward flight. This can be explained by the reduction in drag from the wings as the hawkmoth's flying speed increases (see Figure 14 (e-f)). During 4 m/s forward flight, the hawkmoth

produces less drag than it does during hovering and 2 m/s forward flight, and as a result, its cycle-averaged mechanical power is lower. In addition, our results also shed the insights that the speed limit in hawkmoth forward flying seems not directly related to the high power consumption in high-speed flight. This is consistent with a recent particle image velocimetry study of hawkmoth forward flight (Warfvinge, KleinHeerenbrink et al. 2017), which also found at the power requirements of flight at the maximum sustained wind tunnel flight speed was less than that of hovering flight. Table 3 also shows that the hawkmoth produces slightly less lift as its flight speed increases. This is a result of the negative lift production during the upstroke at higher forward flying speeds.

Table 3. Cycle-averaged lift, mechanical power (with 100% elastic storage), lift-to-power ratio, mass-specific aerodynamic power ($\bar{\boldsymbol{P}}^*_{\boldsymbol{aero}}$), inertial power ($\bar{\boldsymbol{P}}^*_{\boldsymbol{iner}}$), 100% elastic mechanical power ($\bar{\boldsymbol{P}}^*_{\boldsymbol{mech,100\%}}$), and 0% elastic mechanical power ($\bar{\boldsymbol{P}}^*_{\boldsymbol{mech,0\%}}$) for hovering (0 m/s), slow forward flight (2 m/s), and fast forward flight (4 m/s).

Cycle-averaged Values	**Hovering**	**Slow Forward Flight**	**Fast Forward Flight**
Lift (mN)	16.38	16.09	15.22
Mechanical Power (mW)	89.45	90.13	81.50
Lift-to-Power Ratio (N/W)	0.18	0.18	0.19
$\bar{P}^*_{aero}$ (W/kg)	51.32	52.87	47.57
$\bar{P}^*_{iner}$ (W/kg)	1.29	0.15	0.37
$\bar{P}^*_{mech,100\%}$ (W/kg)	52.61	53.02	47.94
$\bar{P}^*_{mech,0\%}$ (W/kg)	87.86	81.06	62.83

Next, we compare the vortex structures generated by hawkmoth across three different flight speeds in Figure 16. Five slices cut along the wingspan demonstrate how the different flapping kinematics modulate the LEV at various flight motion. During hovering flight, a strong LEV is formed and attached well on the wing surface during both the downstroke and upstroke. At both forward flying speeds, a larger LEV is present during the downstroke (e.g. at t/T=0.25 in Figure 16), while a smaller LEV is present during the upstroke (e.g. at t/T=0.75 in Figure 16). To take a close look at the LEV formation with different flight motion, we present both three-dimensional and two-dimensional views of slice cut at the mid-downstroke (Figure 17) and mid-upstroke (Figure 18).

Figure 17 depicts the vortex structures at t/T=0.25, and it includes vectors to show the direction of net force at different forward flying speeds during the hawkmoth's downstroke. This figure shows that as the hawkmoth's flight speed increases, the net force vector during the downstroke becomes increasingly vertical. As a result, the drag produced during the downstroke is minimized, as shown graphically in Figure 14 (c). We hypothesize that this minimization of drag may be attributed to flight stability requirements at higher forward flying speeds. The instantaneous momentum at higher flying speed is much higher than that at lower speed. So, the hawkmoth not only needs to maintain a cycle-averaged force balance in horizontal direction, but also has to minimize the magnitude of drag force oscillation during each stroke. At higher flight speeds, the hawkmoth must limit instantaneous drag force magnitude during its downstroke to keep itself from blowing away in the incoming flow. In order to do so, the hawkmoth must keep its wing pitching angle roughly parallel to the incoming flow when flying at higher forward flight speeds, as seen in Figure 13.

Figure 18 shows the mid-upstroke vortex structures and net force vectors for hovering 2 m/s forward flight, and 4 m/s forward flight. During the hovering upstroke, the wing pitch angle is more vertical, and the net force is angled upward. During the forward flight upstroke, however, the wing pitch angle is more horizontal, and the net force vector is angled down. As a result, lift is generated during the hovering upstroke but not during the forward flight upstroke, as shown graphically in Figure 14. We hypothesize that due to biological limitations, a hawkmoth cannot drastically alter its wing kinematics as it transitions from downstroke to upstroke. As a result, the horizontal wing orientation observed during a forward flying hawkmoth's downstroke is also present during its upstroke. This may explain why the hawkmoth's upstroke is used to generated positive lift during hovering flight but significant amount of negative lift force generation were observed during 2 m/s and 4 m/s forward flight.

Among all three simulations, we observed two separate LEV above the hawkmoth wing at 2 m/s forward flight, as shown in Figure 19. This phenomenon is also known as a dual LEV and has been observed throughout 1 m/s and 2 m/s hawkmoth flight by Johansson et al.(Johansson, Engel et al. 2013). For the current study, the dual LEV was only visible during the upstroke for the 2 m/s forward flying hawkmoth, but not for the 4 m/s case.

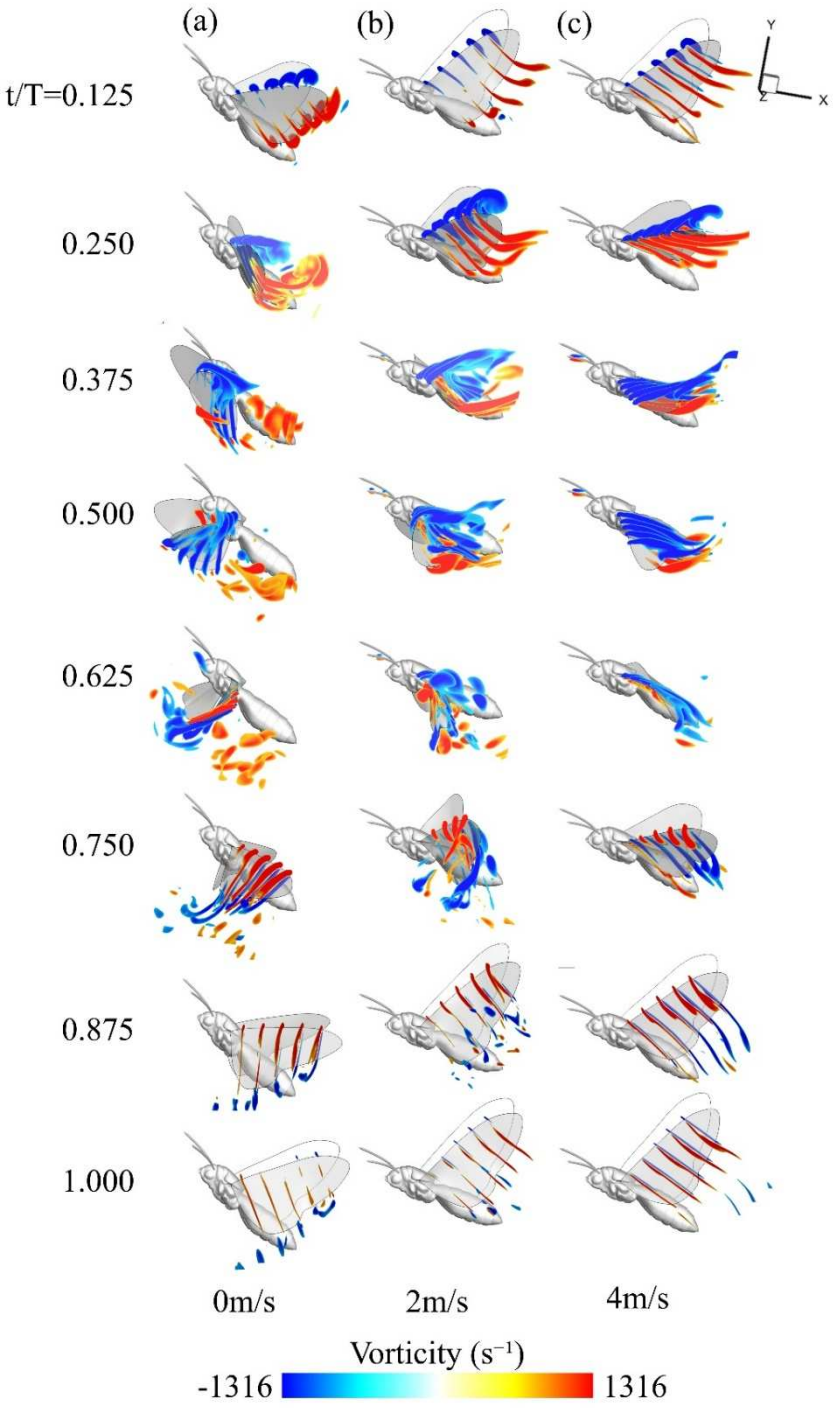

Figure 16. Wing slices throughout one wingbeat cycle for (a) hawkmoth hovering, (b) 2 m/s forward flight, and (c) 4 m/s forward flight. A total of five slices were taken at 0.11R, 0.28R, 0.44R, 0.60R, and 0.77R.

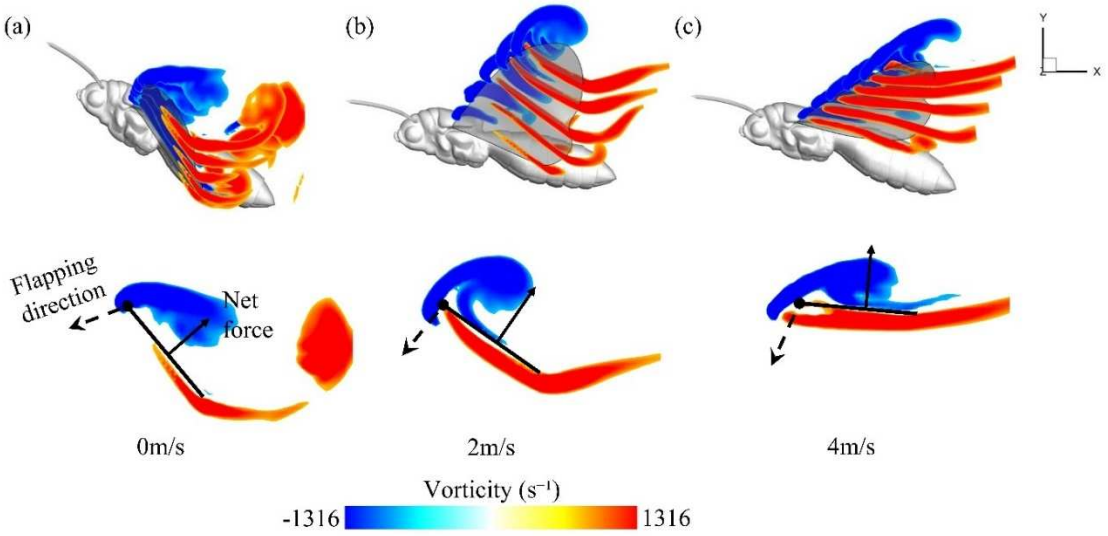

Figure 17. Three-dimensional and two-dimensional views of slice cut vortex structures at mid-downstroke (t/T=0.25) for (a) hawkmoth hovering, (b) 2 m/s forward flight, and (c) 4 m/s forward flight. The 2D view is shown for the chord located at 0.60R. Net force vectors and arrows representing flapping direction are also included. The black circle is located along the wing's leading edge.

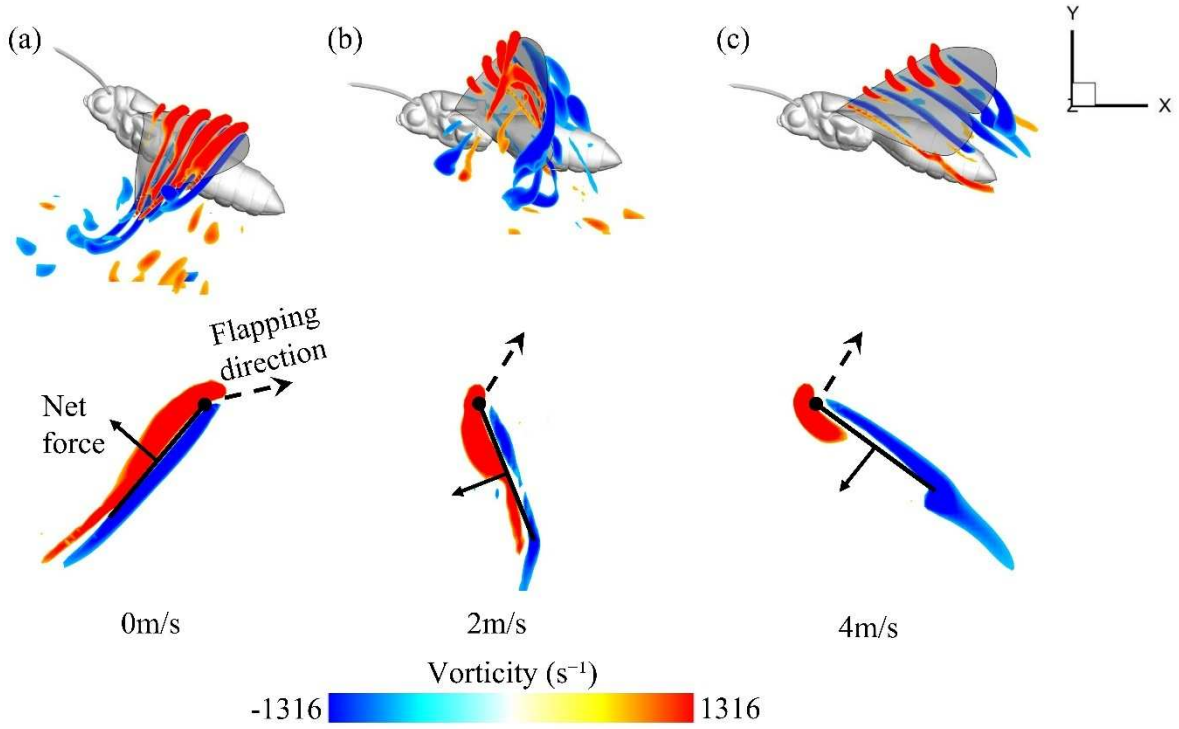

Figure 18. Three-dimensional and two-dimensional views of slice cut vortex structures at mid-upstroke (t/T=0.75) for (a) hawkmoth hovering, (b) 2 m/s forward flight, and (c) 4 m/s forward flight. The 2D view is shown for the chord located at 0.60R. Net force vectors and arrows representing flapping direction are also included. The black circle is located along the wing's leading edge.

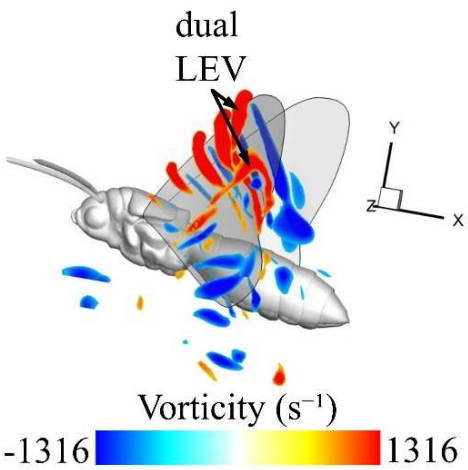

Figure 19. Dual LEV is observed for the hawkmoth forward flight at 2m/s forward flight. The time instant for this picture is at t/T=0.79, around the mid-upstroke.

In addition to the visualization of the vortex structures near the wing surface, we also present the far wake structures. Figure 20 shows the time sequence for the flow field at hovering, 2 m/s forward flight, and 4 m/s forward flight. The vortex structures were plotted using the iso-surface of the Q-criterion. For each flight speed, a strong LEV is formed during the downstroke. A tip vortex and trailing edge vortex can also be observed.

As one can expect, the downwash is located directly below the hawkmoth's body during hawkmoth hovering flight. At 2 m/s forward flight, the downwash is situated both below and behind the hawkmoth. When the flight speed increase to 4 m/s, a chain of vortex tubes is observed behind the insect body. This change in wake structures can be explained by a combination of flight speed and the induced flow generated by flapping wings at each flight speed. As the hawkmoth's flight speed increases, the wing kinematics shift from a 'back-and-forth' motion to an 'up-and-down' motion. During 4 m/s forward flight, the

hawkmoth's wing pitching angle is roughly parallel to the incoming flow. Combining with such a high forward flying speed, vortices are shed directly behind the hawkmoth.

Figure 21 shows the vortex structures present at mid-downstroke (t/T=0.25) for hovering, 2 m/s forward flight, and 4 m/s forward flight. The downstroke for all three flight speeds is accompanied by the formation of a large LEV and TV. A TEV is also present during the downstroke for all three flapping cases. However, for 4 m/s forward flight, the size of the TEV is significantly smaller than for hovering and 2 m/s forward flight. Zheng et al. (Zheng, Hedrick et al. 2013) and Aono et al. (Aono, Shyy et al. 2009) have noted that during hovering flight, the LEV, TV, and TEV form a horseshoe-shaped pattern around the hawkmoth wing during the downstroke. For the current study, this pattern can be clearly observed during hovering and 2 m/s flight, but the much smaller TEV for 4 m/s flight prevents the formation of a full horseshoe pattern. This can be partially explained by the stretching and distortion of the vertex structures due to the strong convection at 4 m/s.

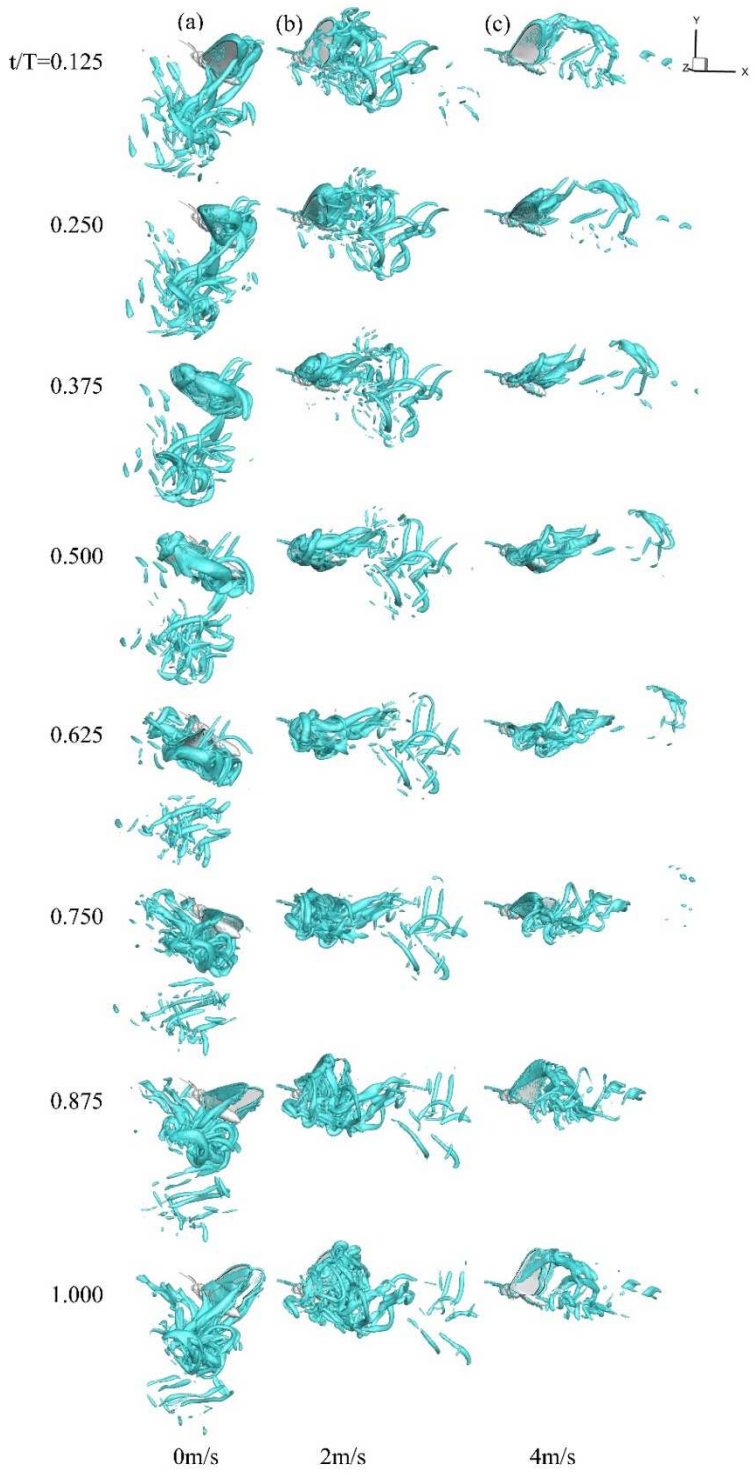

Figure 20. Q-criterion vortex structures for (a) hawkmoth hovering, (b) 2 m/s forward flight, and (c) 4 m/s forward flight. See movie 1 in the supplementary material for simulated flow animations.

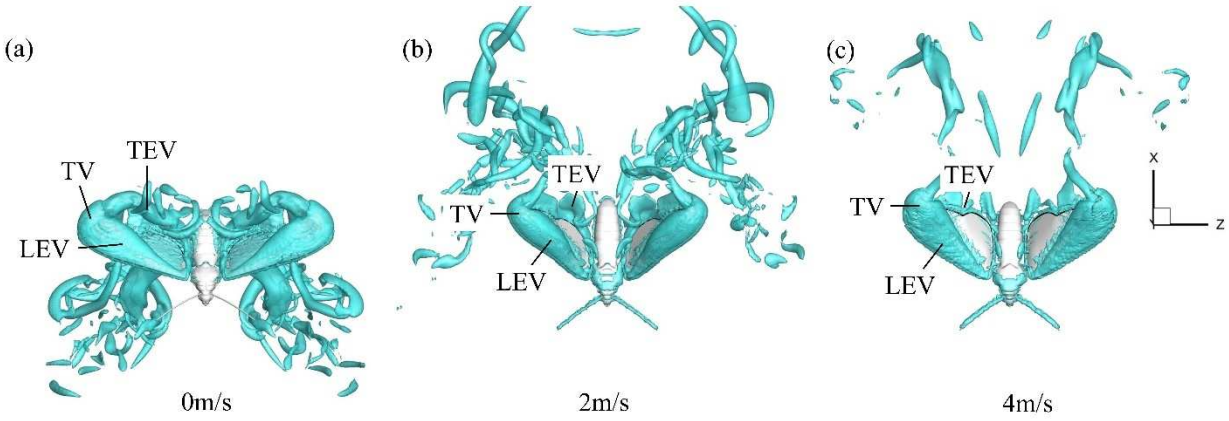

Figure 21. Top view of vortex structure generated at the mid-downstroke (t/T=0.25) for (a) hawkmoth hovering, (b) 2 m/s forward flight, and (c) 4 m/s forward flight.

Next, we visualize the distribution of lift force generation on the wing surface. Figure 22 shows mean lift production on the wing surface during the downstroke and upstroke, respectively, for all simulated flight motions. Lift production during the hovering downstroke increases along the wingspan, with the highest amount of lift produced near the wing tip and the lowest lift produced near the wing root. However, during the downstroke for the forward flying cases, the greatest lift is produced along the leading edge of the wing, and the lowest lift is produced along the trailing edge. We believe that this difference is linked to the location of the maximum flow velocity for each flight case. During hovering flight, the maximum flow velocity is generated by the wing tip, resulting in the greatest lift generation near this region. However, during forward flight, the flapping wing encounters the incoming flow which will enhance the development of the LEV along the wingspan. In addition, as the flying speed gradually increases, hawkmoths tilt the stroke plane more vertically, which further promotes lift generation during the downstroke. As a

result, there is a larger LEV along the spanwise portion of the wing, and a greater portion of the overall lift is generated during the forward flight downstroke.

The most significant difference on the lift generation between hovering and forward flight appears during the upstroke. The hovering upstroke is similar to the hovering downstroke, with lift production increasing along the wingspan, resulting in greatest lift close to the wing tip. However, the lift production during the forward flight upstroke displays an opposite pattern. For 2 m/s and 4 m/s forward flight, significant negative lift is produced near the wing tip, while slight amount of positive lift production is seen close to the wing root. This reversal of lift production during the upstroke is evidence for a different mechanism of lift production for hovering compared to forward flight. For both 2 m/s and 4 m/s forward flight, approximately 75% of the wing surface produces negative lift during the upstroke. This observation is reflected in Figure 14 (b-c), which shows positive lift generation during both the upstroke and negative lift generation during the upstroke for 2 m/s and 4 m/s forward flight. However, during the hovering upstroke, the entire wing surface shows positive lift production. This corresponds to Figure 14 (a), which shows that during the hovering upstroke, positive lift is generated during both the upstroke and downstroke.

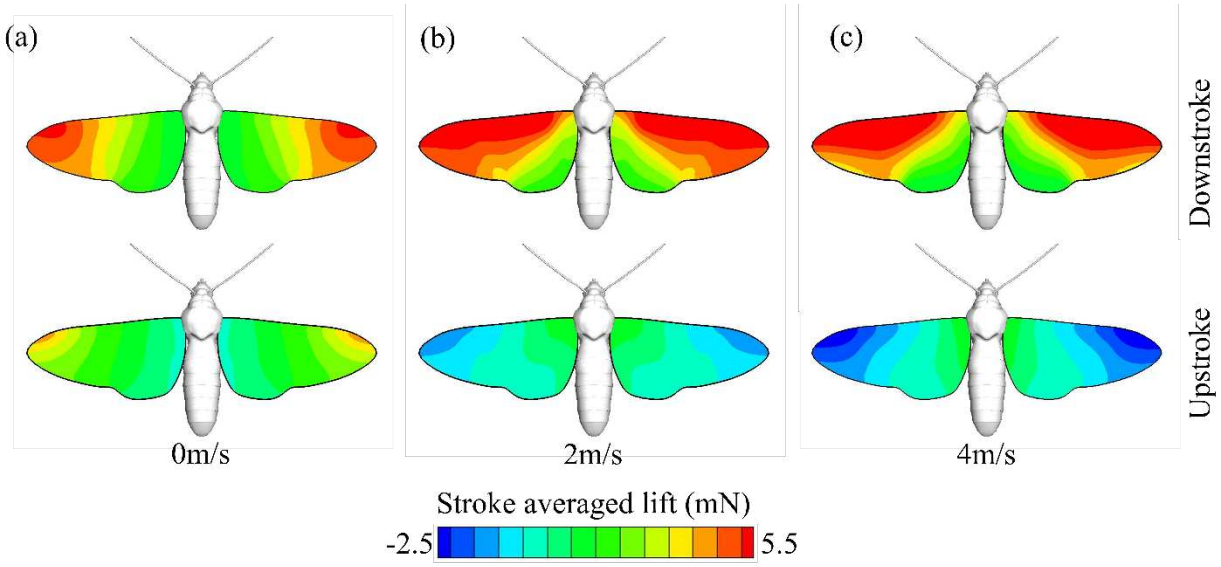

Figure 22. Mid-downstroke (t/T=0.25) and mid-upstroke (t/T=0.75) wing surface lift production for (a) hovering, (b) 2 m/s forward flight, and (c) 4 m/s forward flight.

3.3 Comparison of Hawkmoths and Other Flying Animals

We have observed that as the hawkmoth's advance ratio J increases along with flight speed, lift production is increasingly dominated by the downstroke. At hovering (J=0), both the downstroke and upstroke provide positive contributions to the total lift generation for the flapping cycle. However, at 2 m/s (J=0.41) and 4 m/s (J=0.85) forward flight, the downstroke produces 100% of the overall lift, and negative lift is generated during the upstroke.

Several previous studies (Dudley and Ellington 1990, Dudley and Ellington 1990, Sun and Wu 2003, Wan, Dong et al. 2015) have also commented on the relationship between an insect's advance ratio and the downstroke's contribution to total lift production. The results of the current study are qualitatively consistent with results obtained by Sun &

Wu (Sun and Wu 2003) for a model fruit fly. They found that for an advance ratio of 0.13, the downstroke contributes 75% of the total lift production. For an advance ratio of 0.53, the downstroke contributes 100% of the total lift, and negative lift is generated during the upstroke. Dudley & Ellington (Dudley and Ellington 1990) also found that for a relatively high advance ratio of 0.59, 100% of a bumblebee's total lift is produced during the downstroke, but they did not indicate whether the upstroke generates negative lift in their study.

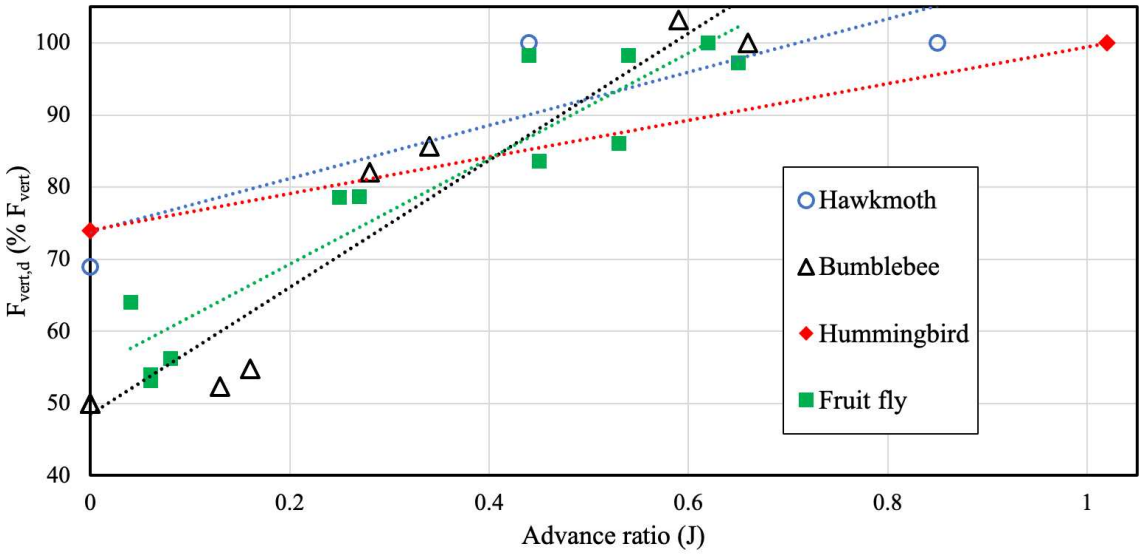

Figure 23. Relationship between the advance ratio (J) and $F_{vert,d}$ (% F_{vert}) for different small animal species, including hawkmoth (current study), bumblebee (Dudley and Ellington 1990, Dudley and Ellington 1990), hummingbird (Song, Luo et al. 2014, Song, Tobalske et al. 2016), and fruit fly (Zhu and Sun 2020). Least-squares trendlines are shown as dashed lines for each species.

Following the definition presented in the literature (Dudley and Ellington 1990), we evaluated the percentage of the vertical force generated during the downstroke ($F_{vert,d}$) over the vertical force generated during the entire cycle (F_{vert}) as a function of the advance ratio (J) across different species. Figure 23 shows the relationship between the J and $F_{vert,d}$ (% F_{vert}) for a variety of small flying animals. This plot shows that as an animal's advance ratio increases, the downstroke plays an increasingly important role in the overall lift production. The plot also shows that if the advance ratio is sufficiently high, the downstroke generates 100% of the total lift. In addition, a least-squares trendline is included for each species. Comparing the results for each species shows that as a flying animal's weight increases, the slope of this trendline generally decreases.

Based on the results from the current study, we suspect that maximum flying speed limitation is due to changes in a flying animal's wing kinematics as its advance ratio increases. As the flight speed gradually increases, the animal must find a way to minimize drag during its entire flapping cycle to prevent itself from blowing away in the incoming flow. To minimize the magnitude of the instantaneous drag force generated during the downstroke, the animal has to reduce its wing pitching angle by orienting its wings roughly parallel to the flow direction, while still maintain sufficient angle of attack for lift generation. As the advance ratio continuously increases with flight speed, a significant amount of negative lift force starts to appear during the upstroke resulting from a negative angle of attack. As a consequence, the positive lift generated during the animal's downstroke is not sufficient to overcome the body weight together with the negative lift generated during the upstroke. However, increasing downstroke lift would also increase downstroke drag, requiring more upstroke thrust and resulting in more upstroke negative

lift. Thus, these kinematic limitations result in a limit to its maximum forward flying speed as we and others observe in wind tunnel flight studies. Compared to birds and bats, insects are more strongly limited by these effects because they cannot reconfigure their wings during the stroke cycle. For example, birds typically flex their wings at the wrist joint during upstroke, reducing wing span and area (Tobalske and Dial 1996). Despite having inflexible wings in comparison to most other bird species, even hummingbirds exhibit such an ability and increasingly reduce wing span during upstroke as flight speed increases (Tobalske, Warrick et al. 2007). Insects have no such ability, and thus might generally exhibit lower maximum flight speeds than flying vertebrates of similar wing loading.

In addition, forward flying hummingbirds produce thrust during their downstroke by maintaining a negative wing pitch angle (Song, Tobalske et al. 2016). In this study, we observed that hawkmoths minimize their pitch angle as flight speed increases, and they therefore produce very little thrust at higher flight speeds. Other studies have similarly shown that in general, flying insects are unable to generate thrust during their downstroke (Wan, Dong et al. 2015, Li and Dong 2017, Zhu and Sun 2020). This difference between flying insects (e.g. hawkmoths) and flying vertebrates (e.g. hummingbirds) may be attributed to the musculoskeletal structure found in vertebrate wings. Hummingbirds use their skeletons to exert fine control over their wing kinematics during the downstroke, which enables them to generate thrust. However, due to their lack of a skeletal structure, hawkmoths and other flying insects do not possess this ability.

Chapter 4: Ctenophore Swimming

In this chapter, the hydrodynamic performance of a forward-swimming ctenophore is evaluated. Ctene thrust generation and tip vortex formation are discussed in detail. To determine the effects of tip vortex interactions, the original reconstruction is compared to a modified low-density ctene row. In addition, ctene performance and vortex structures are presented for different values of *Re*. Finally, effects of substrate curvature are discussed.

4.1 Ctenophore Swimming Kinematics

Morphological and kinematic measurements of the ctenophore used in this study are briefly presented here. Table 4 summarizes several key parameters, including phase lag (P_L = 11.20%), stroke angle (Φ = 100.50°), and ctene beat frequency (f = 13.04). These values are consistent with previous studies on similarly sized ctenophores (Herrera-Amaya, Seber et al. 2021). The oscillatory Reynolds number (Re_ω = 30.00) is intermediate, which indicates that both viscous and inertial forces play a role in ctene propulsion. Figure 24 shows the average tip velocity U_{tip} for the middle eight ctenes (this includes ctenes e-l, as shown in Figure 7). The power stroke is shaded gray and constitutes approximately half of the total beat cycle.

Table 4. Morphological and kinematic measurements of the ctenophore used in this study. Standard deviation is included for average values.

L_b (mm)	κ (m^{-1})	U_b (mm/s)	l (mm)	P_L (%)	Φ (°)	f (Hz)	Re_ω	Re_b
11.56	169.15	7.35	0.62 ± 0.02	11.20	100.50	13.04	30.00	80.87

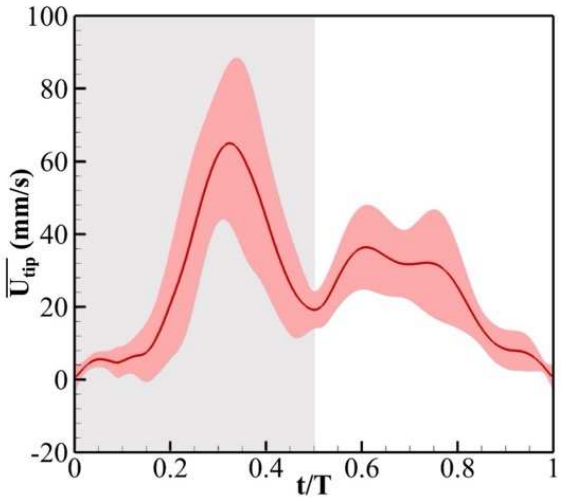

Figure 24. Average tip velocity for the middle eight ctenes (e-l). Standard deviation is shown in pink, and the power stroke is shaded gray.

4.2 Ctene Hydrodynamics

The in-house CFD solver was used to evaluate the hydrodynamic performance of the ctene row reconstruction shown in Figure 7. The instantaneous thrust produced by each of the sixteen appendages is plotted in Figure 25. This plot illustrates how a ctene's force generation changes throughout its power stroke and recovery stroke. During the power stroke, thrust peaks as the ctene straightens and sweeps forward. During the recovery stroke, some drag is generated as the ctene deforms and returns to its original position. Due to the spatiotemporal asymmetry of the beat cycle (Herrera-Amaya, Seber et al. 2021), the amount of thrust produced by a ctene's power stroke is typically greater than the drag produced by its recovery stroke. Figure 25 also shows how thrust production is affected by metachronal paddling. Due to the phase lag between appendages, a ctene's thrust starts to peak just as an adjacent ctene's thrust begins to decrease. Therefore, at all times throughout

the beat cycle, at least one of the ctenes is contributing to thrust production. This effect may be likened to the functioning of a sixteen-cylinder engine, in which torque is maintained by the sequential firing of the sixteen pistons.

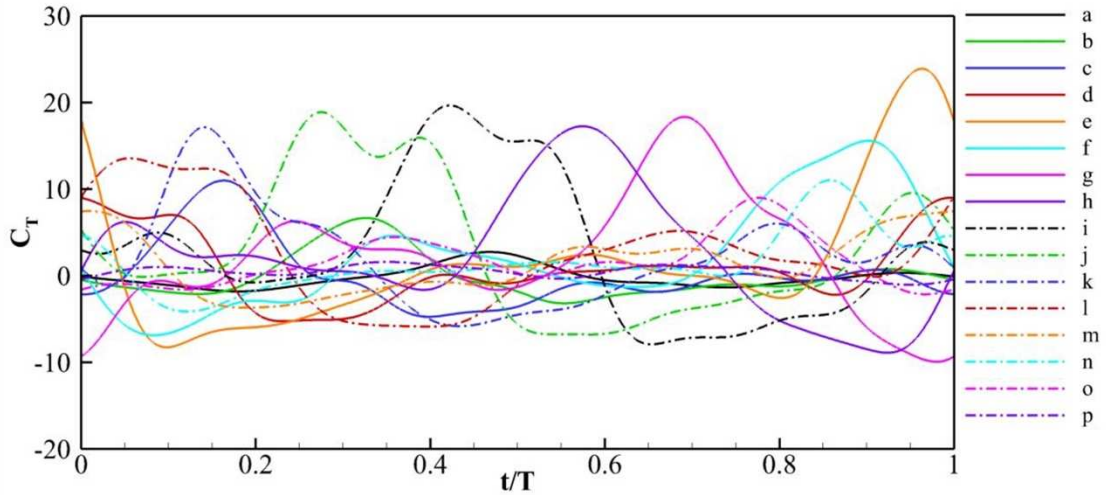

Figure 25. Instantaneous thrust generation by all sixteen ctenes throughout one beat cycle.

Figure 26 shows the vorticity produced by the row throughout the beat cycle. As a ctene enters its power stroke, a positive red vortex forms at its tip. This positive vortex contributes to the ctene's thrust generation (Kim and Gharib 2011). Next to the positive tip vortex, a negative blue shear layer is created as adjacent ctenes perform their recovery stroke. This negative shear layer enhances the drag produced by the recovering ctenes. To illustrate the life cycle of these vortices, Figure 26 identifies two locations along the row where a negative shear layer can be observed. These regions of negative vorticity are labelled v1 and v2. At t/T = 0.25, v1 is located near the bottom of the row, and v2 is located near the top. As the beat cycle progresses, v1 and v2 travel through the row as different ctenes perform their recovery strokes. v1 grows stronger as it nears the middle of the row,

while v2 weakens and disappears as it nears the top of the row. Ctene beating is shown to be cyclic, because at t/T = 1.00, v2 is located approximately where v1 was located at the start of the beat cycle. In this fashion, positive tip vortices and negative shear layers travel through the row as part of a metachronal wave. Figure 27 shows in detail the vortices produced by the row at t/T = 1.00. In this figure, ctene f is in the middle of its power stroke and features a positive tip vortex (v). Upstream from this vortex, ctene e generates a smaller positive vortex (v_u); downstream, recovering ctenes g-i produce a negative shear layer (v_d). This demonstrates that as tip vortices travel through the ctene row, they undergo complex interactions with corotating and counterrotating neighboring vortices. In the next section, we determine whether these interactions are constructive or destructive, and we examine how they affect ctene hydrodynamic performance.

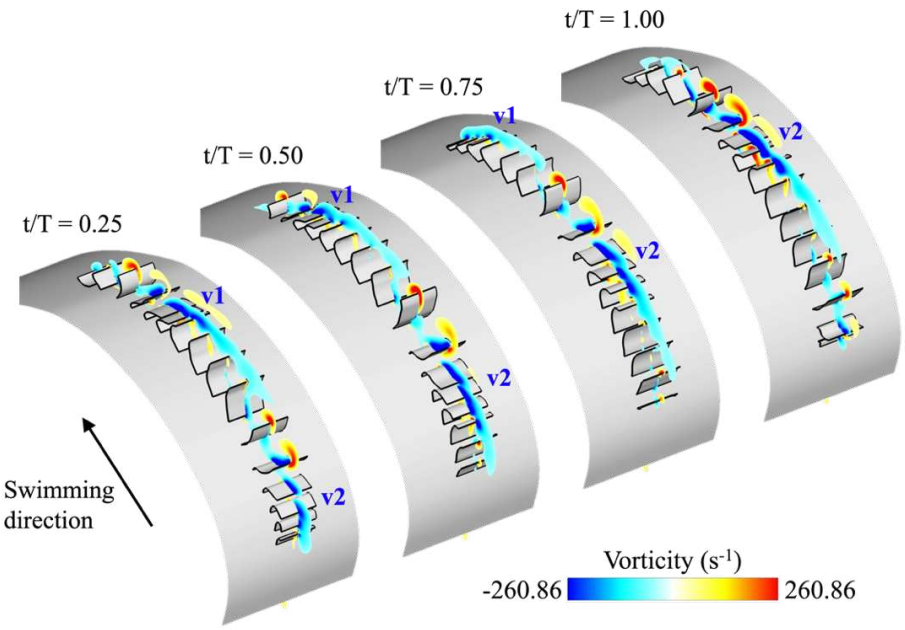

Figure 26. Time sequence of vorticity throughout one beat cycle. Negative shear layers are labelled v1 and v2. The swimming direction of the ctenophore is also labelled. The swimming direction is the same for subsequent figures.

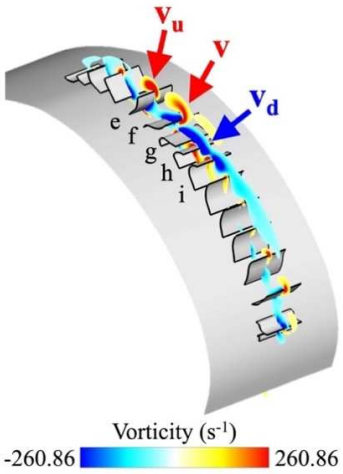

Figure 27. Vortices produced by the ctene row at t/T = 1.00. As ctene f performs its power stroke, it generates a tip vortex, labelled v. Upstream and downstream vortices are labelled v_u and v_d, respectively.

4.3 Vortex Interaction Mechanism

Previous studies have suggested that vortex interactions between adjacent metachronal appendages may improve hydrodynamic performance (Ford and Santhanakrishnan 2021, Ford and Santhanakrishnan 2021). To determine the mechanism of these interactions, we created a low-density simulation case that features a greater distance between appendages. This increased distance enabled the observation of ctene hydrodynamics minus the effects of vortex interactions. The low-density case was a modification of the original reconstruction and was formed by removing every other ctene along the row. As a result, the low-density case approximately doubles the space between adjacent appendages. In total, eight ctenes (b, d, f, h, j, l, n, and p) were removed, and original kinematics were preserved for the remaining eight. The vorticity produced by this

low-density case is shown in Figure 28. As previously observed, a positive tip vortex is formed as ctenes perform their power stroke. However, due to the increased distance between appendages, recovering ctenes generate distinct negative vortices rather than a full shear layer.

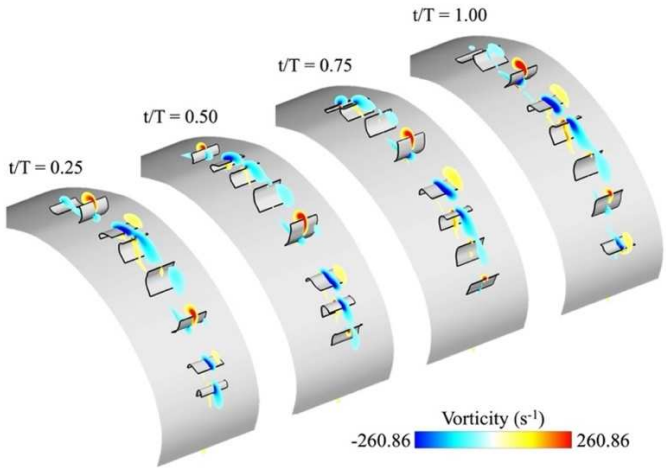

Figure 28. Time sequence of vorticity generated by the low-density case throughout one beat cycle.

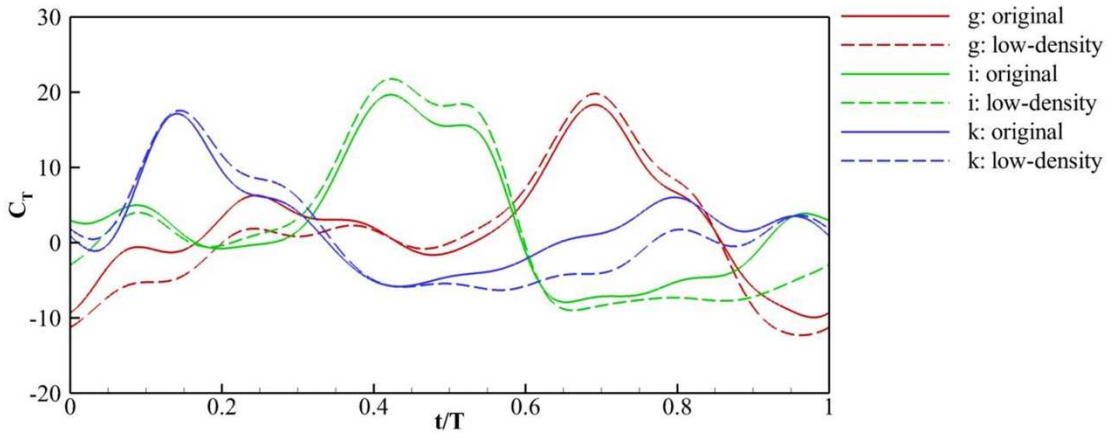

Figure 29. Instantaneous thrust generation by ctenes g, i, and k. Results are shown for the original case and the low-density case.

Figure 29 shows the instantaneous thrust produced by ctenes g, i, and k. Results are included for the original case and the low-density case. Both cases show that the beat cycle is divided between a thrust-producing power stroke and a drag-producing recovery stroke. However, in the low-density case, ctenes generate slightly more thrust during the power stroke and significantly more drag during the recovery stroke. This indicates that increasing the distance between appendages yields a greater magnitude of horizontal force production throughout the beat cycle. To explain why this occurs, Figure 30 compares the two cases (original and low-density) using several snapshots of the vorticity field around ctene i. At $t/T = 0.52$, ctene i is in the middle of its power stroke and features a positive tip vortex. This positive vortex is clearly smaller in the original case than in the low-density case, which explains why the original case generates slightly less thrust during the power stroke. A similar effect can be observed during the recovery stroke. At $t/T = 0.96$, the negative vortex attached to ctene i appears smaller in the original case than in the low-density case. This explains why the original case generates significantly less drag during the recovery stroke.

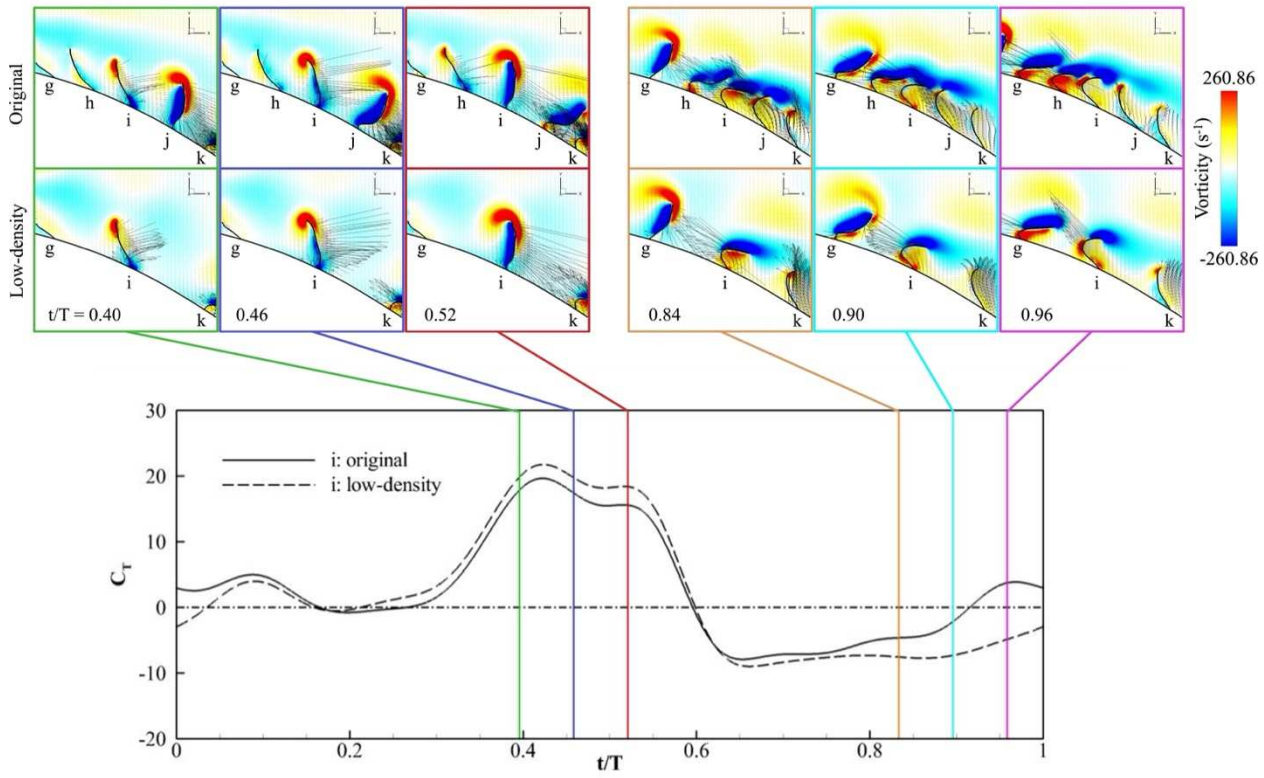

Figure 30. Comparison between the original case and the low-density case. Vorticity and velocity vectors are shown at various instances during ctene i's power stroke and recovery stroke.

Figure 31 shows the cycle-averaged thrust generation, power consumption, and efficiency (C_T/C_{PW}) for each ctene. Results are presented for the original case and the low-density case. As shown in 31(a), ctenes in the original case generate more thrust, which can be attributed to the proposed vortex-weakening mechanism. This mechanism significantly reduces drag generation during the recovery stroke, which outweighs the slight decrease in thrust during the power stroke. As a result, overall thrust generation is improved. 31(a) also shows that the larger ctenes near the middle of the row produce the most thrust, and the first few ctenes in the row (a and b in the original case) produce a small

amount of drag. 31(b) displays the average power consumption for each ctene. This plot shows that ctenes in the original case consume less power, which is another benefit of the vortex-weakening mechanism. This mechanism reduces the magnitude of instantaneous thrust production throughout the beat cycle, and as a result, ctenes consume less power (calculated as the product of velocity and hydrodynamic force). 31(c) shows the average efficiency for each ctene. The original case is more efficient than the low-density case. In both cases, the first few ctenes in the row are the least efficient, and the last few ctenes are the most efficient. Table 5 reports the cycle-averaged average thrust generation, power consumption, and efficiency for the entire ctene row. These values were calculated by averaging the performance of each of the sixteen ctenes within the row. Compared to the original row, the low-density row generates 41.45% less thrust, consumes 31.89% more power, and is 62.07% less efficient. The superior performance of the original row is a result of the previously discussed ctene tip vortex interactions.

Based on these observations, we hypothesize that in natural ctenophore swimming, ctene tip vortices are weakened due to destructive interactions with neighboring vortices. As ctenes beat metachronally, they move apart during the power stroke and move toward each other during the recovery stroke. Therefore, destructive tip vortex interactions are minimized during the power stroke and are maximized during the recovery stroke. Because the recovery stroke is responsible for drag generation, this vortex-weakening mechanism enhances ctene hydrodynamic performance.

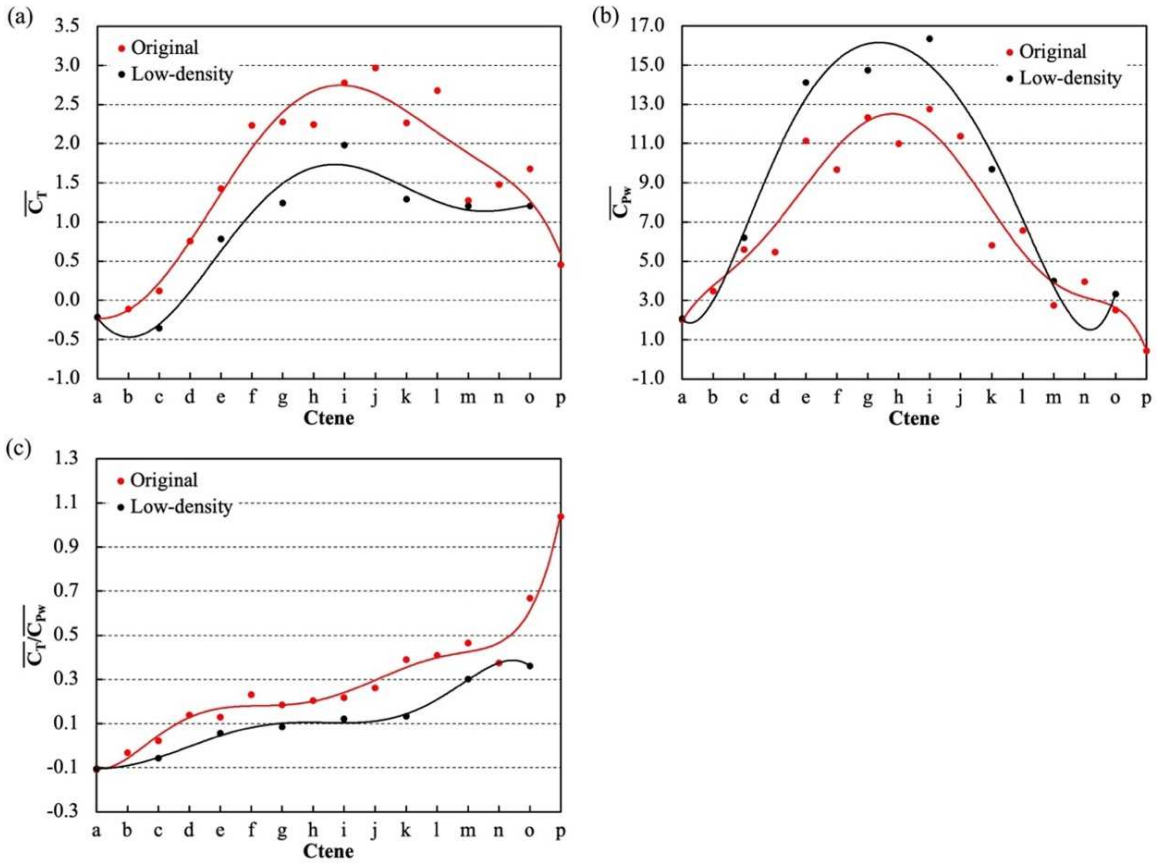

Figure 31. Cycle-averaged (a) thrust generation, (b) power consumption, and (c) efficiency values for each ctene along the row. Results are shown for the original case and the low-density case.

Table 5. Average ctene row performance for the original case and the low-density case. Values were calculated by averaging the performance all sixteen ctenes within the row.

	$\overline{C_T}$	$\overline{C_{PW}}$	$\overline{C_T}/\overline{C_{PW}}$
Original case	1.52	6.68	0.29
Low-density case	0.89 (↓ 41.45%)	8.81 (↑ 31.89%)	0.11 (↓ 62.07%)

4.4 Effects of Varying the Reynolds Number

Ctenophores are the largest animals that locomote via ciliary propulsion (Matsumoto 1991). In this section, we examine how this propulsion mechanism functions across a range of flow regimes. The previously described original and low-density cases were run with $Re_\omega = 30$, which was calculated using real ctene kinematics. For this section, four additional cases were simulated with artificially large values of Re_ω. Using the original ctene row, two simulations were run with $Re_\omega = 60$ and $Re_\omega = 120$. Using the low-density row, another two simulations were run with $Re_\omega = 60$ and $Re_\omega = 120$. Instantaneous thrust results for these cases are reported in Figure 32. 32(a) shows the thrust produced by ctenes g, i, and k in the original row. As Re_ω increases, less thrust is generated during the power stroke, and less drag is generated during the recovery stroke. In other words, the magnitude of horizontal force production is reduced throughout the beat cycle. 32(b) displays similar results for the low-density row. To explain this trend, Figure 33 shows how varying Re_ω affects the vortex wake structures produced by the ctene row. When $Re_\omega = 30$, tip vortices remain attached to the beating ctenes. However, when $Re_\omega = 120$, vortices are shed into the wake. In natural ctenophore swimming ($Re_\omega = 30$), tip vortices enhance ctene force production. Therefore, vortex shedding at higher Re_ω reduces the magnitude of thrust generation, as observed in Figure 32.

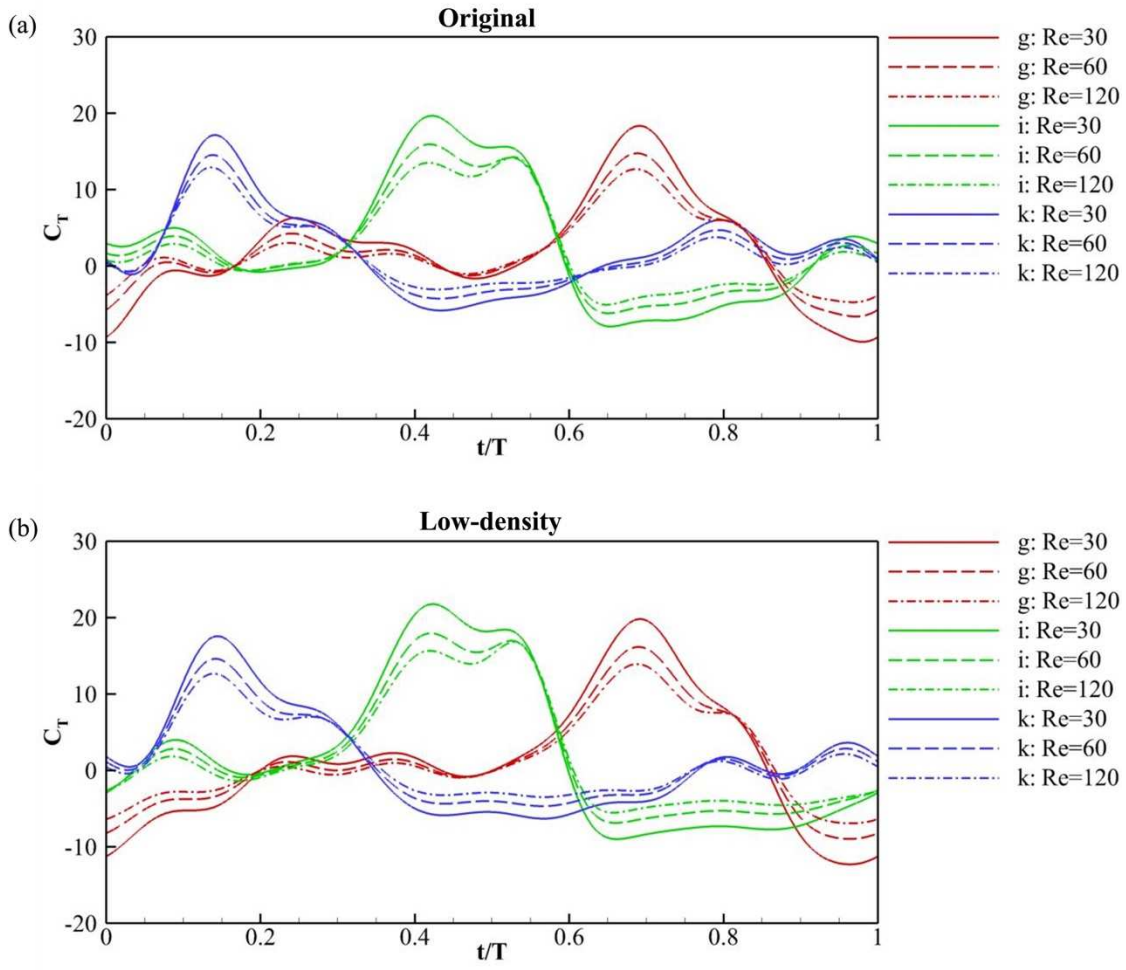

Figure 32. Instantaneous thrust generation by ctenes g, i, and k at different Reynolds numbers (Re=30, Re=60, Re=120). Results are shown for (a) the original ctene row and (b) the low-density row.

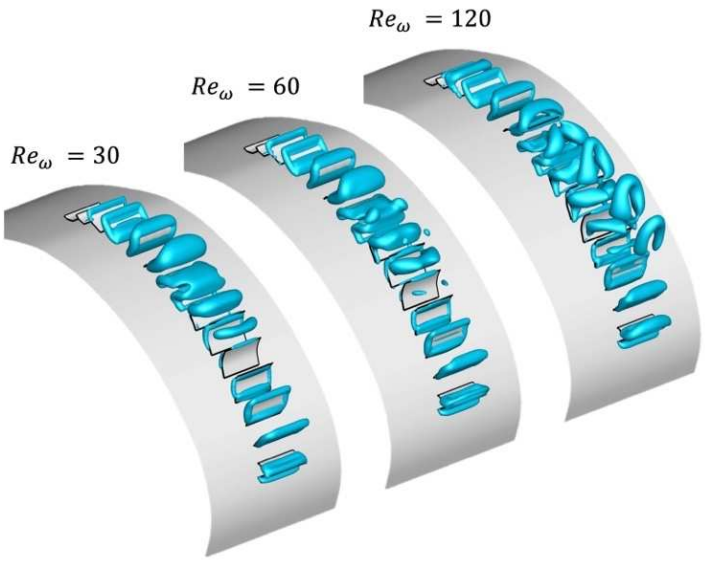

Figure 33. Q-isosurface vortex structures generated by the original ctene row at t/T=1.00. Results are shown for $Re_\omega = 30$, $Re_\omega = 60$, and $Re_\omega = 120$.

Figure 34 shows how Re_ω affects cycle-averaged ctene performance. For ctenes in the original row, average thrust production and power consumption decrease as Re_ω becomes larger. The decrease in thrust generation is caused by tip vortex shedding, and the decrease in power consumption is a result of the thinner boundary layer at higher Re_ω. Due to this decrease in power consumption, ctene efficiency (C_T/C_{PW}) improves slightly as Re_ω becomes larger. The low-density ctene row exhibits similar trends in power consumption and efficiency. However, unlike the original row, average thrust generation remains relatively unchanged by increasing Re_ω. This difference is a result of the proposed vortex-weakening mechanism. In the original row, destructive vortex interactions reduce the amount of drag produced by recovering ctenes. When tip vortices are shed at higher Re_ω, this drag-reducing effect is lost and ctenes therefore generate less average thrust. The low-density ctene row does not benefit from tip vortex interactions, and as a result, its average

thrust generation is not affected by varying Re_ω. These trends are summarized in Table 6, which shows the average ctene row performance for each case. As Re_ω increases, the original row produces less thrust, consumes less power, and becomes slightly more efficient. The low-density row similarly consumes less power and becomes more efficient. However, for reasons described above, its thrust generation is not affected by changing Re_ω.

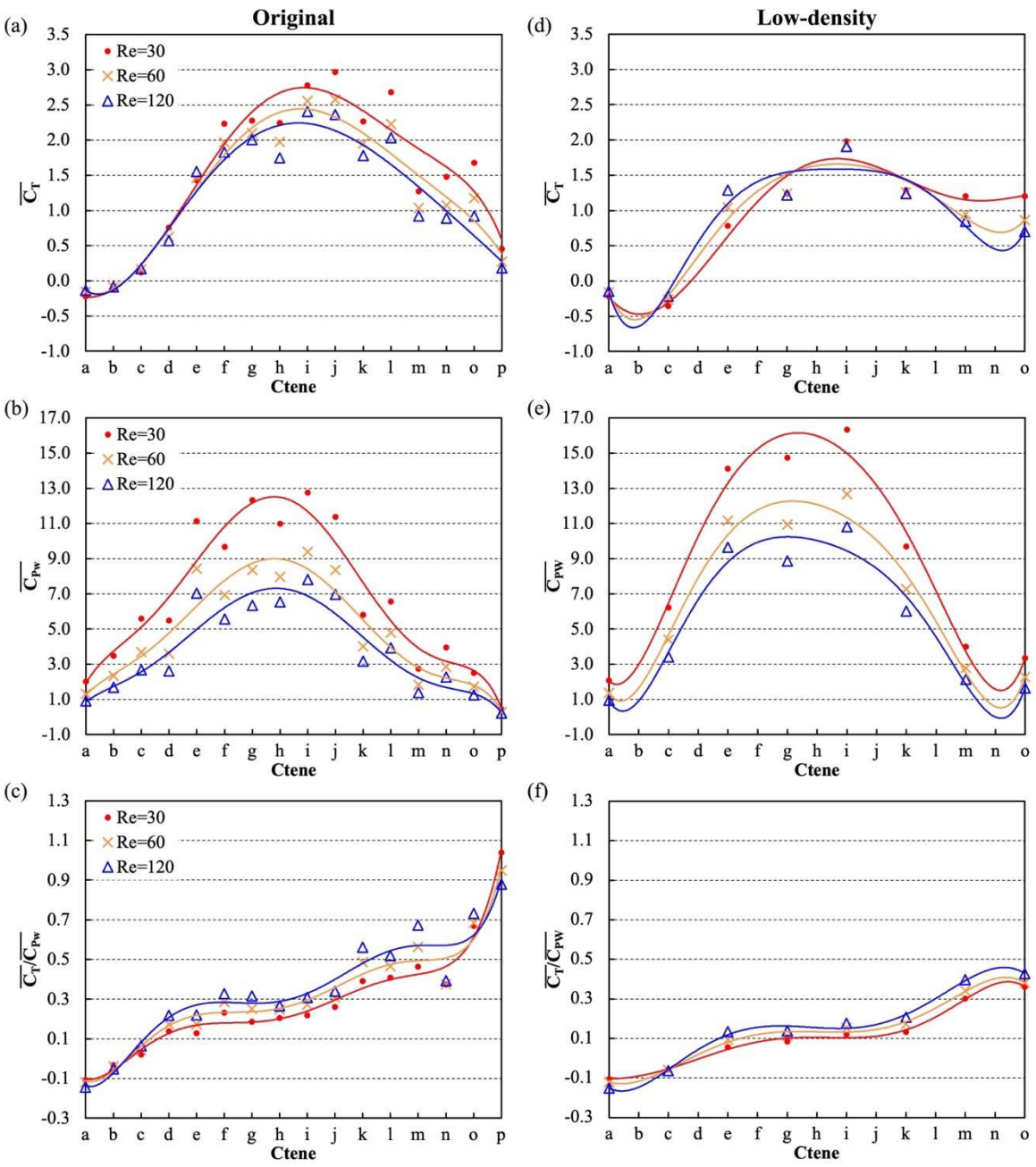

Figure 34. Cycle-averaged thrust, power, and efficiency for each ctene. Results are shown for $Re_\omega = 30$, $Re_\omega = 60$, and $Re_\omega = 120$. The left column (a-c) includes results for the original ctene row, and the right column (d-f) includes results for the low-density row.

Table 6. Average ctene row performance for different values of Re_ω. Results are presented for the original ctene row and the low-density row.

		$\overline{C_T}$	$\overline{C_{PW}}$	$\overline{C_T}/\overline{C_{PW}}$
Original row:	$Re_\omega = 30$	1.52	6.68	0.29
	$Re_\omega = 60$	1.31 (↓ 13.82%)	4.74 (↓ 29.04%)	0.32 (↑ 10.34%)
	$Re_\omega = 120$	1.20 (↓ 21.05%)	3.78 (↓ 43.41%)	0.35 (↑ 20.69%)
Low-density row:	$Re_\omega = 30$	0.89	8.81	0.11
	$Re_\omega = 60$	0.86 (↓ 3.37%)	6.60 (↓ 25.09%)	0.13 (↑ 18.18%)
	$Re_\omega = 120$	0.86 (↓ 3.37%)	5.44 (↓ 38.25%)	0.16 (↑ 45.45%)

4.5 Effects of Varying Substrate Curvature

Most previous studies on ciliary hydrodynamics have assumed that cilia are embedded in a completely flat substrate. However, in nature, the bodies of ctenophores and other ciliated invertebrates are nontrivially curved (Tamm 2014). To determine how body curvature affects ctene hydrodynamics, we progressively flattened the model substrate used in this study. We ran simulations using four different substrate curvatures, including the original curvature, 66% curvature, 33% curvature, and flat. Figure 35 shows a perspective view and a side view of these geometries, and their calculated curvatures are included in Table 7. For each substrate geometry, simulations were run using both the original ctene row and the low-density row. Figure 36 shows the vorticity produced by the original row along each of the different substrate curvatures. As previously observed,

ctenes generate a positive vortex during their power stroke, and they generate a negative shear layer during their recovery stroke. These vortex formations are consistent across all four substrate curvatures. Figure 37 displays similar results for the low-density ctene row.

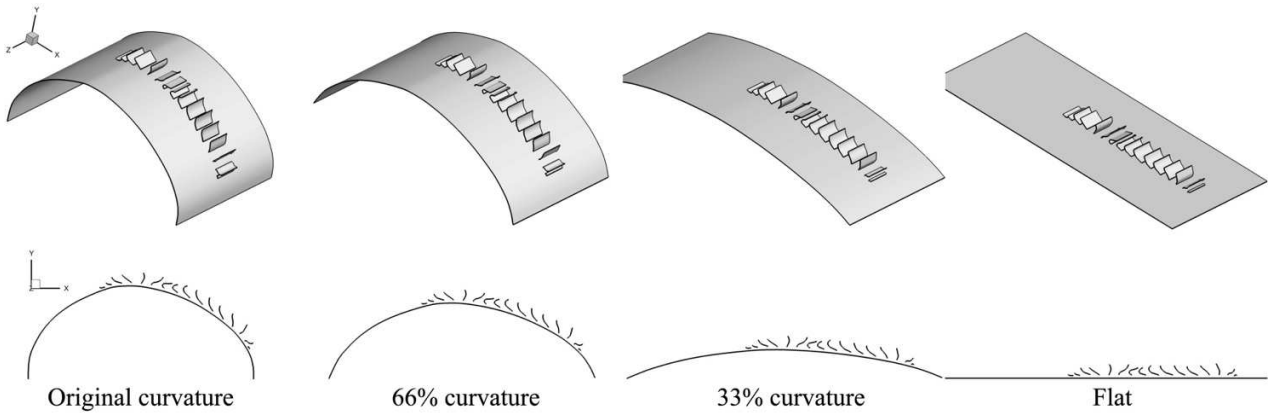

Figure 35. Perspective view (top) and side view (bottom) of the different substrate geometries.

Table 7. Calculated curvature for each substrate geometry.

	κ (m^{-1})
Original curvature	169.15
66% curvature	119.65
33% curvature	41.20
Flat	0.00

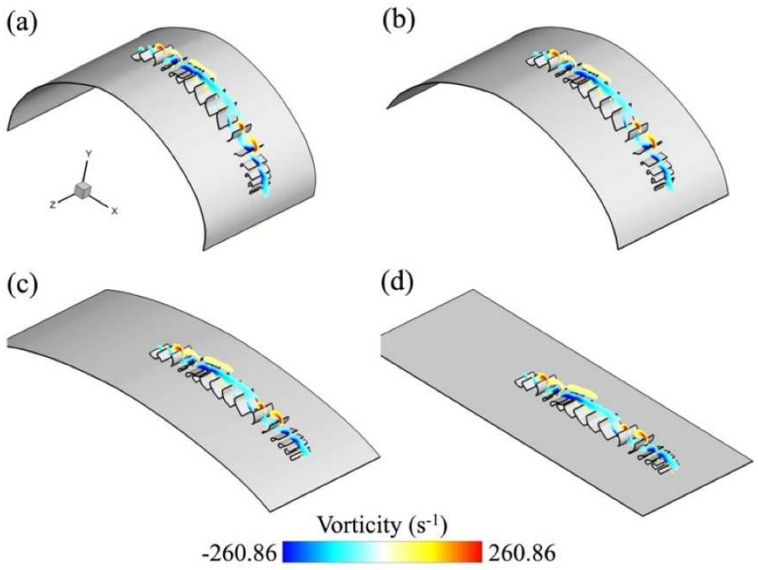

Figure 36. Vorticity generated by the original ctene row at t/T = 0.25. Results are shown for different substrate curvatures, including (a) the original curvature, (b) 66% curvature, (c) 33% curvature, and (d) flat.

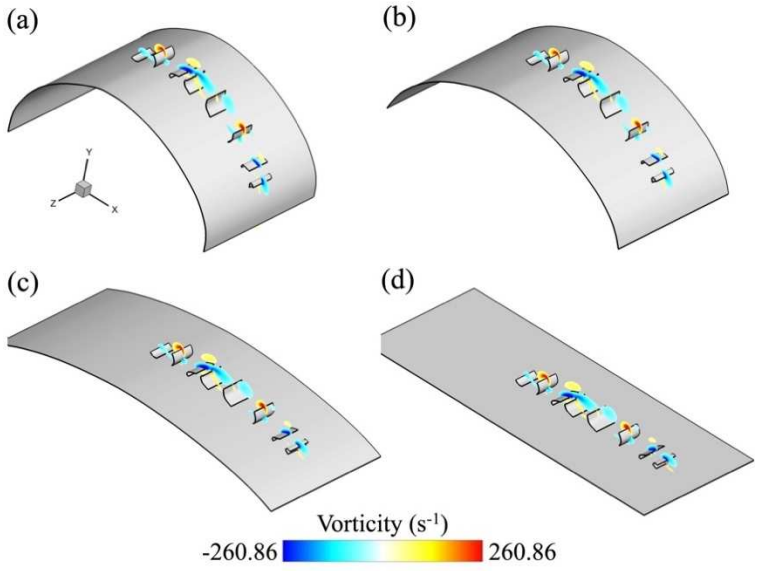

Figure 37. Vorticity generated by the low-density ctene row at t/T = 0.25. Results are shown for different substrate curvatures, including (a) the original curvature, (b) 66% curvature, (c) 33% curvature, and (d) flat.

Figure 38 shows the cycle-averaged ctene performance for each substrate curvature. 38(a) includes the average thrust produced by ctenes in the original row. For the first four ctenes (a-d), the original curvature generates less thrust than the other three curvatures. However, for the remaining twelve ctenes (e-p), the original curvature generates significantly more thrust. 38(b) shows the average lift produced by ctenes in the original row. For the first five ctenes (a-e), all curvatures generate approximately the same amount of lift. However, for the other eleven ctenes (f-p), the original curvature produces less lift than the other curvatures. Average total force generation, shown in 38(c), remains unchanged by substrate curvature. Similar trends are observed for the low-density row, as seen in 38(d-f). In addition, Figure 39 shows that as the substrate flattens, ctene power consumption remains unchanged and ctene efficiency decreases. These trends are summarized in Table 8 and Table 9. Table 8 shows that as the substrate flattens, the ctene row generates more thrust and less lift, while its total force production is relatively unaffected. Table 9 shows that the ctene row consumes the same amount of power and becomes less efficient. These trends are observed for both the original ctene row and the low-density row, which suggests that the proposed vortex-weakening mechanism is not affected by substrate curvature.

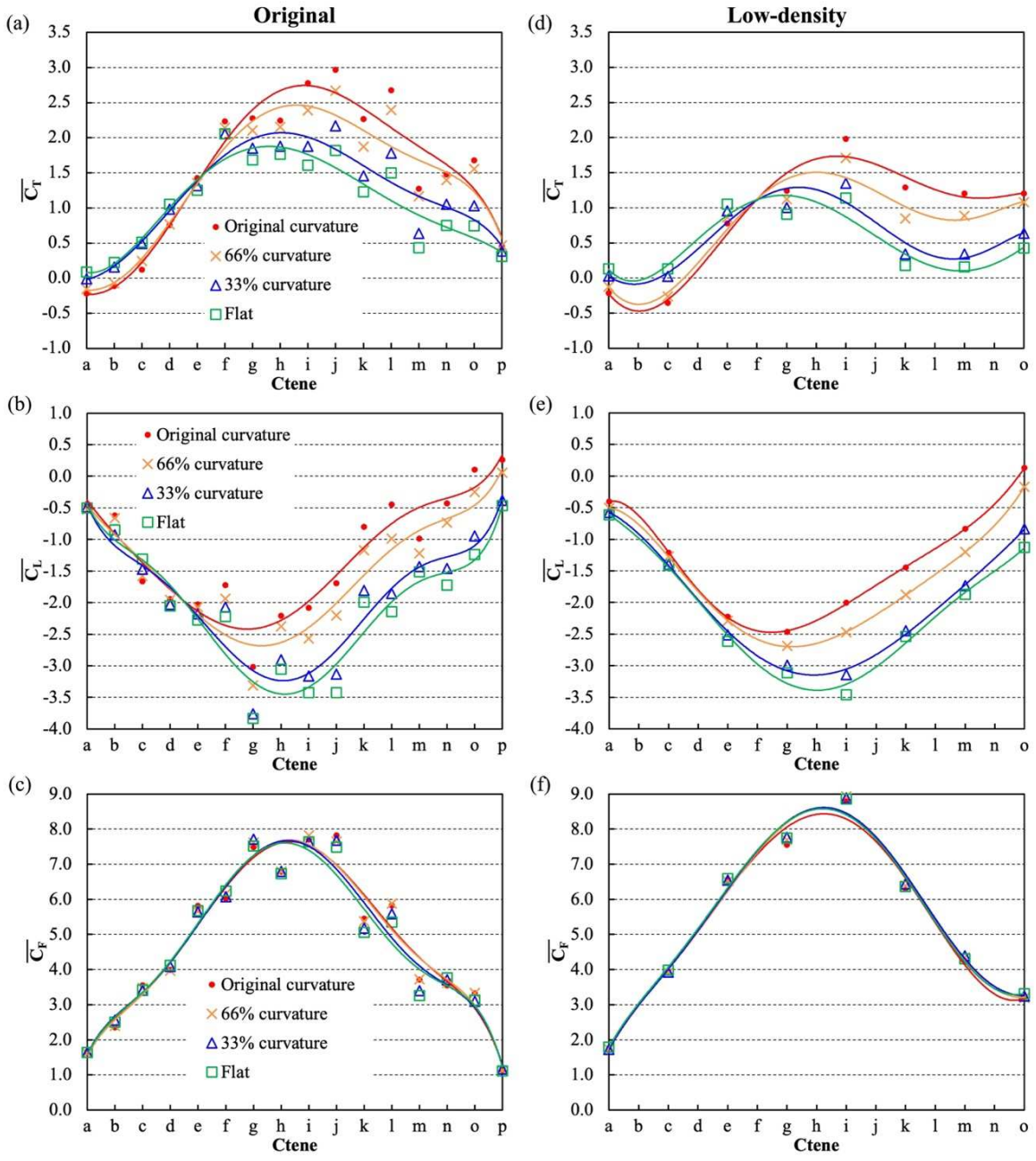

Figure 38. Cycle-averaged ctene force generation for each substrate curvature. Results are shown for the original ctene row (a-c) and the low-density row (d-f).

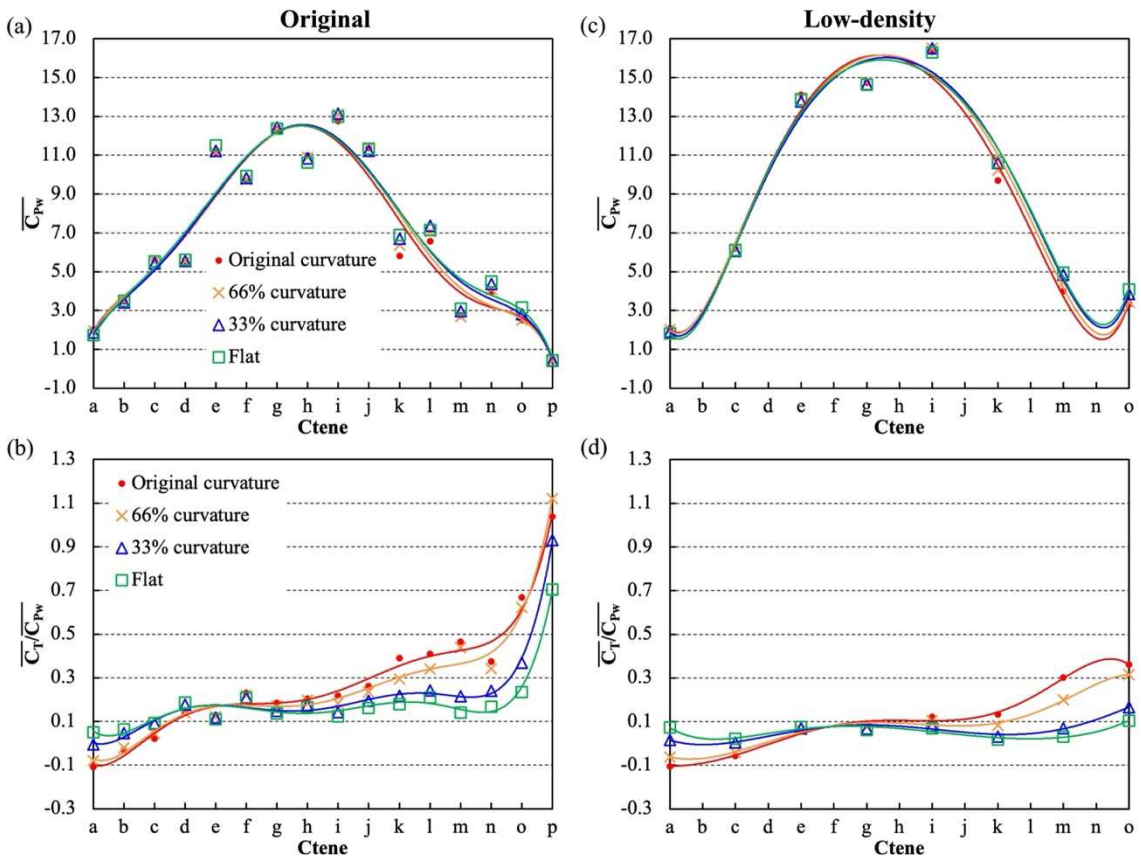

Figure 39. Cycle-averaged ctene power consumption and efficiency for each substrate curvature. Results are shown for the original ctene row (a,b) and the low-density row (c,d).

Table 8. Average ctene row force generation for different substrate curvatures. Results are presented for the original ctene row and the low-density row.

		$\overline{C_T}$	$\overline{C_L}$	$\overline{C_F}$
Original row:	Original curvature	1.52	-1.23	4.76
	66% curvature	1.40 (↓ 7.89%)	-1.47 (↑ 19.51%)	4.76 (– 0.00%)
	33% curvature	1.20 (↓ 21.05%)	-1.87 (↑ 52.03%)	4.71 (↓ 1.05%)
	Flat	1.06 (↓ 30.26%)	-2.00 (↑ 62.60%)	4.66 (↓ 2.10%)
Low-density row:	Original curvature	0.89	-1.31	5.28
	66% curvature	0.77 (↓ 13.48%)	-1.56 (↑ 19.08%)	5.34 (↑ 1.14%)
	33% curvature	0.58 (↓ 34.83%)	-1.95 (↑ 48.85%)	5.37 (↑ 1.70%)
	Flat	0.52 (↓ 41.57%)	-2.09 (↑ 59.54%)	5.37 (↑ 1.70%)

Table 9. Average ctene row power consumption and efficiency for different substrate curvatures. Results are presented for the original ctene row and the low-density row.

		$\overline{C_{PW}}$	$\overline{C_T}/\overline{C_{PW}}$
Original row:	Original curvature	6.68	0.29
	66% curvature	6.77 (↑ 1.35%)	0.27 (↓ 6.90%)
	33% curvature	6.85 (↑ 2.54%)	0.22 (↓ 24.14%)
	Flat	6.90 (↑ 3.29%)	0.18 (↓ 37.93%)
Low-density row:	Original curvature	8.81	0.11
	66% curvature	8.94 (↑ 1.48%)	0.092 (↓ 16.36%)
	33% curvature	9.02 (↑ 2.38%)	0.063 (↓ 42.73%)
	Flat	9.05 (↑ 2.72%)	0.057 (↓ 48.18%)

We observed that total ctene force production and power consumption are not affected by substrate curvature. We therefore conclude that varying the curvature affects ctenophore hydrodynamic performance simply by reorienting the direction of ctene motion. To illustrate how this occurs, Figure 40 shows the average thrust and lift vectors for each ctene along the different substrate curvatures. Most of the ctenes along the original substrate are oriented roughly parallel to the ctenophore's direction of motion. As a result, their beating generates a significant amount of thrust. In contrast, ctenes along the flat substrate are oriented more perpendicular to the ctenophore's direction of motion. This explains why ctenes along the flat substrate generate mostly lift. In ctenophore forward swimming, lift does not contribute to propulsion. Due to the symmetrical arrangement of

ctene rows around the ctenophores body, lift generated by one row is negated by the row located directly across the body. Because the original substrate curvature generates the least lift and most thrust, it provides the best hydrodynamic performance of the four curvatures tested. It is worth noting that the first few ctenes along the original curvature generate a slight amount of drag, thereby reducing the performance of the entire row. However, these ctenes may be needed to produce the vortex-weakening mechanism discussed in the previous sections.

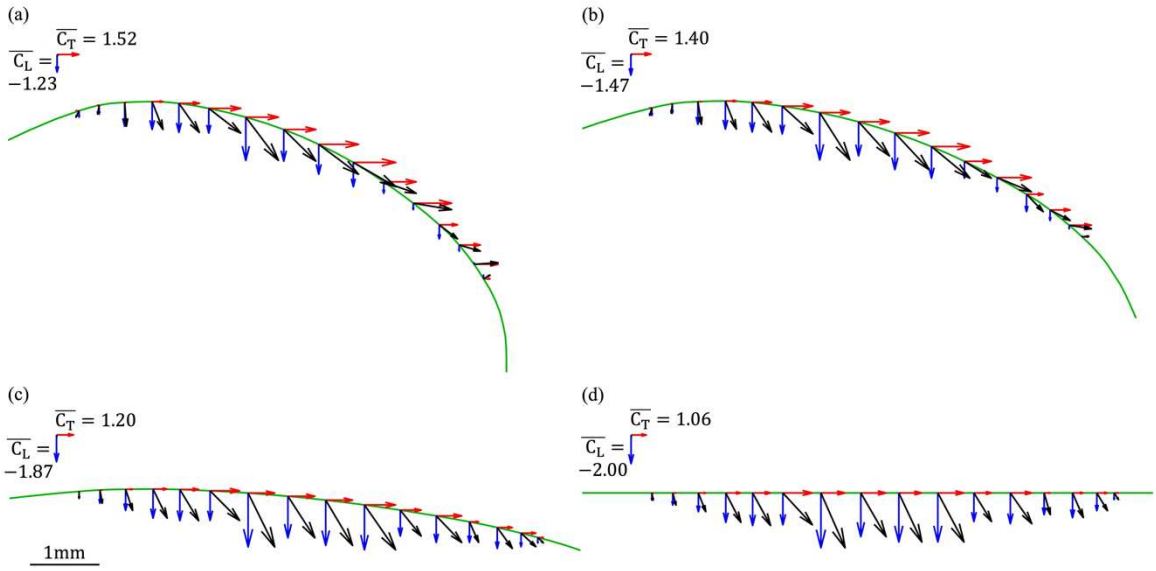

Figure 40. Vector diagram showing the average thrust and lift produced by each ctene. Thrust vectors are colored red, and lift vectors are colored blue. Results are shown for different substrate curvatures, including (a) the original curvature, (b) 66% curvature, (c) 33% curvature, and (d) flat. Average ctene row force vectors are shown above each curvature.

Chapter 5: Summary and Conclusions

In this thesis, hawkmoth forward flight and ctenophore swimming were simulated using an in-house immersed-boundary-method-based CFD solver. Key findings are summarized below.

5.1 Hawkmoth Flight Conclusions

We have numerically investigated the unsteady aerodynamics of hawkmoth flight across a range of flying speeds (0 m/s – 4 m/s). Flapping wing kinematics of hawkmoths have been reconstructed using high-speed wind tunnel recordings. An in-house immersed-boundary-method-based CFD solver has been used to simulate hawkmoth's flight. Results show that as the hawkmoth transitions from hovering to forward flight, the hawkmoth's stroke plane angle increases and its upstroke wing pitch angle decreases. These kinematic changes lead to differences in aerodynamic force production and power consumption between hovering and forward flight.

During hawkmoth hovering, significant lift is generated during both the downstroke and upstroke, with the downstroke contributing around 72% of the total lift. At 2 m/s and 4 m/s forward flight, however, the downstroke provides all of the lift, and negative lift is generated during the upstroke. Detailed analysis has been performed on the vortex formation and force destructions on the wing surfaces. Our results indicated that the power consumption seem not to restrict forward flight speed in hawkmoths. Instead, the hawkmoth has to manage drag during its downstroke to prevent large, unstable body oscillations at higher forward flying speeds. To reduce drag force generated during each downstroke, the forward flying hawkmoth must maintain a small wing pitching angle that

is roughly parallel to the flying direction. Due to biological limitations, the hawkmoth cannot drastically alter its wing pitching angle during the short period of the wing reversal. As a result, a forward flying hawkmoth's wings have to remain approximately horizontal respect to the stroke plane during the upstroke, which lead to a negative lift force generation. As the flying speed increases, the lift generated during the downstroke cannot balance with the body weight together with the negative lift generated during the upstroke. This effect limits high speed flight in hawkmoths, and highlights the importance of reconfigurable wings to the wide range of flight speeds achieved by flying vertebrates.

5.2 Ctenophore Swimming Conclusions

In this study, we simulated ctenophore swimming kinematics using an in-house immersed-boundary-method-based CFD solver. Simulation results show that ctenes form a thrust-producing tip vortex during their power stroke and a drag-producing shear layer during their recovery stroke. As ctenes beat metachronally, these vortices interact to enhance the net thrust generation. We propose that this enhancement occurs via destructive interactions between neighboring vortices. Ctenes move apart during their power stroke and move toward each other during their recovery stroke. As a result, destructive vortex interactions are minimized during the power stroke and are maximized during the recovery stroke. This has the effect of slightly reducing thrust generation and significantly reducing drag generation. As a result, this vortex-weakening mechanism increases overall thrust production, decreases power consumption, and improves efficiency.

Ctene tip vortex dynamics are strongly affected by Reynold's number. As *Re* increases, ctenes shed their tip vortices into the wake, and as a result, their thrust production decreases. In addition, the boundary layer thins as *Re* increases, which reduces ctene power

consumption. This reduction in power consumption results in slightly higher efficiency for higher *Re*.

In nature, ctenophores can possess a wide variety of different body morphologies. To determine how body geometry affects ctene performance, we ran several simulations using different body curvatures. Results show that by having a curved substrate, ctenophores orient their ctenes roughly parallel to their direction of motion. This has the effect of increasing thrust generation and decreasing lift generation.

5.2 Future Work

The following recommendations are made for future work:

1. It was concluded that hawkmoths cannot fly faster than 4m/s due to biological limitations. It may be helpful to directly compare hawkmoth wing kinematics with similarly sized species capable of faster flight speeds (e.g. hummingbirds). Such a comparison would demonstrate how other species are able to avoid the natural limitations of hawkmoth flight.
2. In our investigation of ctenophore swimming, the ctene row contained eighteen ctenes. It is currently unknown how many ctenes are necessary to produce the drag-reducing mechanism described in this study. Future studies can determine the effects of reducing the number of ctenes in the row.
3. The ctenophore in this study swam using antiplectic metachronal rowing. This means that the metachronal wave travels from the back to the front of the ctenophore's body. Future studies can examine the effects of symplectic rowing, wherein the metachronal wave travels from the front to the back of the body.

Bibliography

Afzelius, B. r. A. (1961). "The fine structure of the cilia from ctenophore swimming-plates." The Journal of Cell Biology **9**(2): 383-394.

Alben, S., et al. (2010). "Coordination of multiple appendages in drag-based swimming." Journal of The Royal Society Interface **7**(52): 1545-1557.

Aono, H., et al. (2008). "Near- and far-field aerodynamics in insect hovering flight: an integrated computational study." Journal of experimental biology **211**(2): 239-257.

Aono, H., et al. (2009). "Near wake vortex dynamics of a hovering hawkmoth." Acta Mechanica Sinica **25**(1): 23-36.

Barlow, D., et al. (1993). "Water flows around the comb plates of the ctenophore Pleurobrachia plotted by computer: a model system for studying propulsion by antiplectic metachronism." Journal of experimental biology **177**(1): 113-128.

Dauptain, A., et al. (2008). "Hydrodynamics of ciliary propulsion." Journal of Fluids and Structures **24**(8): 1156-1165.

Dudley, R. and C. Ellington (1990). "Mechanics of forward flight in bumblebees: I. Kinematics and morphology." Journal of experimental biology **148**(1): 19-52.

Dudley, R. and C. Ellington (1990). "Mechanics of forward flight in bumblebees: II. Quasi-steady lift and power requirements." Journal of experimental biology **148**(1): 53-88.

Ellington, C. P., et al. (1996). "Leading-edge vortices in insect flight." Nature **384**(6610): 626-630.

Ford, M. P. and A. Santhanakrishnan (2021). "Closer appendage spacing augments metachronal swimming speed by promoting tip vortex interactions." Integrative and comparative biology **61**(5): 1608-1618.

Ford, M. P. and A. Santhanakrishnan (2021). "On the role of phase lag in multi-appendage metachronal swimming of euphausiids." Bioinspiration & Biomimetics **16**(6): 066007.

Gopalkrishnan, R., et al. (1994). "Active vorticity control in a shear flow using a flapping foil." Journal of Fluid Mechanics **274**: 1-21.

Han, J.-S., et al. (2016). "The advance ratio effect on the lift augmentations of an insect-like flapping wing in forward flight." Journal of Fluid Mechanics **808**: 485-510.

Hedrick, T. L. and T. Daniel (2006). "Flight control in the hawkmoth Manduca sexta: the inverse problem of hovering." Journal of experimental biology **209**(16): 3114-3130.

Hedrick, T. L., et al. (2017). "Flight motor modulation with speed in the hawkmoth Manduca sexta." Journal of insect physiology **96**: 115-121.

Herrera-Amaya, A., et al. (2021). "Spatiotemporal asymmetry in metachronal rowing at intermediate Reynolds numbers." Integrative and comparative biology **61**(5): 1579-1593.

Johansson, L. C., et al. (2013). "Multiple leading edge vortices of unexpected strength in freely flying hawkmoth." Scientific reports **3**(1): 1-5.

Kim, D. and M. Gharib (2011). "Characteristics of vortex formation and thrust performance in drag-based paddling propulsion." Journal of experimental biology **214**(13): 2283-2291.

Lei, M., et al. (2021). "Navigation in odor plumes: How do the flapping kinematics modulate the odor landscape?" AIAA paper, 2021-2817.

Lei, M. and C. Li (2020). "The aerodynamic performance of passive wing pitch in hovering flight." Physics of Fluids **32**(5): 051902.

Li, C. (2021). "Effects of wing pitch kinematics on both aerodynamic and olfactory functions in an upwind surge." Proceedings of the Institution of Mechanical Engineers, Part C: Journal of Mechanical Engineering Science **235**(2): 296-307.

Li, C. and H. Dong (2016). "Three-dimensional wake topology and propulsive performance of low-aspect-ratio pitching-rolling plates." Physics of Fluids **28**(7): 071901.

Li, C. and H. Dong (2017). "Wing kinematics measurement and aerodynamics of a dragonfly in turning flight." Bioinspiration & Biomimetics **12**(2): 026001.

Li, C., et al. (2020). "Tip vortices formation and evolution of rotating wings at low Reynolds numbers." Physics of Fluids **32**(2): 021905.

Li, C., et al. (2015). "Effects of a dynamic trailing-edge flap on the aerodynamic performance and flow structures in hovering flight." Journal of Fluids and Structures **58**: 49-65.

Li, C., et al. (2018). "A balance between aerodynamic and olfactory performance during flight in Drosophila." Nature Communications **9**(1): 1-8.

Li, C., et al. (2020). "Dual functions of insect wings in an odor-guided aeronautic navigation." Journal of Fluids Engineering **142**(3): 030902.

Li, C., et al. (2017). "Computational modeling and validation of human nasal airflow under various breathing conditions." Journal of Biomechanics **64**(7): 59-68.

Li, C., et al. (2019). Passive Pitching Mechanism of Three-Dimensional Flapping Wings in Hovering Flight, San Francisco, CA, USA (ASME 2019) V002T02A043, in Proceedings of the 8th Joint Fluids Engineering Conference on ASME-JSME-KSME 2019, AJKFluids 2019-4639.

Lim, J. L. and M. E. DeMont (2009). "Kinematics, hydrodynamics and force production of pleopods suggest jet-assisted walking in the American lobster (Homarus americanus)." Journal of experimental biology **212**(17): 2731-2745.

Liu, G., et al. (2016). "Vortex dynamics and new lift enhancement mechanism of wing–body interaction in insect forward flight." Journal of Fluid Mechanics **795**: 634-651.

Lyu, Y. Z. and M. Sun (2021). "Power requirements for the hovering flight of insects with different sizes." Journal of insect physiology **134**: 104293.

Matsumoto, G. (1991). Swimming movements of ctenophores, and the mechanics of propulsion by ctene rows. Hydrobiologia, Springer.

Mittal, R., et al. (2008). "A versatile sharp interface immersed boundary method for incompressible flows with complex boundaries." Journal of Computational Physics **227**(10): 4825-4852.

Ortega-Jimenez, V. M., et al. (2013). "Hawkmoth flight stability in turbulent vortex streets." Journal of experimental biology **216**(24): 4567-4579.

Sleigh, M. A. (1976). "Fluid propulsion by cilia and the physiology of ciliary systems." Davies PS, Ed. Perspectives in Experimental Biology **1**: 125-134.

Song, J., et al. (2014). "Three-dimensional flow and lift characteristics of a hovering ruby-throated hummingbird." Journal of The Royal Society Interface **11**(98): 20140541.

Song, J., et al. (2016). "Three-dimensional simulation for fast forward flight of a calliope hummingbird." Royal Society open science **3**(6): 160230.

Stevenson, R., et al. (1995). "Cage size and flight speed of the tobacco hawkmoth Manduca sexta." The Journal of experimental biology **198**(8): 1665-1672.

Sun, M. and J. H. Wu (2003). "Aerodynamic force generation and power requirements in forward flight in a fruit fly with modeled wing motion." Journal of experimental biology **206**(17): 3065-3083.

Tamm, S. L. (2014). "Cilia and the life of ctenophores." Invertebrate Biology **133**(1): 1-46.

Theriault, D. H., et al. (2014). "A protocol and calibration method for accurate multi-camera field videography." Journal of experimental biology **217**(11): 1843-1848.

Tobalske, B. and K. Dial (1996). "Flight kinematics of black-billed magpies and pigeons over a wide range of speeds." J Exp Biol **199**(Pt 2): 263-280.

Tobalske, B. W., et al. (2007). "Three-dimensional kinematics of hummingbird flight." Journal of experimental biology **210**(13): 2368-2382.

Wan, H., et al. (2015). "Computational investigation of cicada aerodynamics in forward flight." Journal of The Royal Society Interface **12**(102): 20141116.

Warfvinge, K., et al. (2017). "The power–speed relationship is U-shaped in two free-flying hawkmoths (Manduca sexta)." Journal of The Royal Society Interface **14**(134): 20170372.

Warrick, D. R., et al. (2005). "Aerodynamics of the hovering hummingbird." Nature **435**(7045): 1094-1097.

Willmott, A. P. and C. P. Ellington (1997). "The mechanics of flight in the hawkmoth Manduca sexta. I. Kinematics of hovering and forward flight." The Journal of experimental biology **200**(21): 2705-2722.

Willmott, A. P. and C. P. Ellington (1997). "The mechanics of flight in the hawkmoth Manduca sexta. II. Aerodynamic consequences of kinematic and morphological variation." The Journal of experimental biology **200**(21): 2723-2745.

Yao, J. and K. Yeo (2020). "Forward flight and sideslip manoeuvre of a model hawkmoth." Journal of Fluid Mechanics **896**.

Zhang, P., et al. (2015). "Paramecia swimming in viscous flow." The European Physical Journal Special Topics **224**(17): 3199-3210.

Zheng, L., et al. (2013). "A multi-fidelity modelling approach for evaluation and optimization of wing stroke aerodynamics in flapping flight." Journal of Fluid Mechanics **721**: 118-154.

Zhu, H. J. and M. Sun (2020). "Kinematics Measurement and Power Requirements of Fruitflies at Various Flight Speeds." Energies **13**(16): 4271.